nature nanotechnology

ARTICLES

https://doi.org/10.1038/s41565-021-00962-9

Amplifying STING activation by cyclic dinucleotide–manganese particles for local and systemic cancer metalloimmunotherapy

Xiaoqi Sun[1,2], Yu Zhang[1], Jiaqian Li[3], Kyung Soo Park[2,4], Kai Han[1,2], Xingwu Zhou[1,2], Yao Xu[1,2], Jutaek Nam[1,2,5], Jin Xu[1,2], Xiaoyue Shi[1,2], Lei Wei[6], Yu Leo Lei[3,7,8] and James J. Moon[1,2,4,8] ✉

Nutritional metal ions play critical roles in many important immune processes. Hence, the effective modulation of metal ions may open up new forms of immunotherapy, termed as metalloimmunotherapy. Here, we demonstrate a prototype of cancer metalloimmunotherapy using cyclic dinucleotide (CDN) stimulator of interferon genes (STING) agonists and Mn^{2+}. We screened various metal ions and discovered specific metal ions augmented STING agonist activity, wherein Mn^{2+} promoted a 12- to 77-fold potentiation effect across the prevalent human STING haplotypes. Notably, Mn^{2+} coordinated with CDN STING agonists to self-assemble into a nanoparticle (CDN–Mn^{2+} particle, CMP) that effectively delivered STING agonists to immune cells. The CMP, administered either by local intratumoural or systemic intravenous injection, initiated robust anti-tumour immunity, achieving remarkable therapeutic efficacy with minute doses of STING agonists in multiple murine tumour models. Overall, the CMP offers a new platform for local and systemic cancer treatments, and this work underscores the great potential of coordination nanomedicine for metalloimmunotherapy.

Immunotherapy is revolutionizing cancer treatment[1–3]; however, only a small subset of patients respond to immunotherapies[4]. The limited patient response rate has been attributed to poor anti-tumour immunity in 'cold' tumours, characterized by a low frequency of pro-inflammatory immune cells and an immunosuppressive network in the tumour microenvironment (TME)[5]. Recent studies have shown that the stimulator of interferon genes (STING) pathway plays critical roles in the initiation of anti-tumour immunity and the conversion of 'cold' tumour into 'hot' tumour[6–9]. Briefly, cyclic GMP-AMP synthase (cGAS) detects damage-associated double-stranded DNA in the cytosol and catalyses the generation of cyclic [G(2′,5′)pA(3′,5′)p] (cGAMP), which serves as the second messenger to activate STING and induce type I interferons (IFNs)[6,10,11]. Preclinical studies with STING agonists have shown promising anti-tumour efficacy[7,8]. Yet, because of their metabolic instability, limited cellular permeability and poor drug-like properties, conventional cyclic dinucleotide (CDN)-based STING agonists are administered intratumourally[12,13]. However, the intratumour (i.t.) route of administration is not applicable for treating metastasis, and i.t. injection of CDN-based STING agonists has produced disappointing results in clinical trials[12,13]. Although new STING agonists based on non-CDN structures have been recently reported for systemic administration[14–17], their toxicity profiles and efficacy are yet to be studied in clinical trials. Alternatively, nanoparticles, such as those based on polymers and liposomes, could augment the local and systemic therapeutic effects of CDN-based STING agonists[9,18–22], thus underscoring the potential and utility of nanomedicine-based delivery of STING agonists.

Emerging evidence has indicated the essential roles of metal ions in immune regulation[23,24], including T cell activation (Ca^{2+})[25,26] and stemness (K^+)[27,28], activation of inflammasome (K^+, Ca^{2+} and Na^+)[29–31], pathogen–host interactions ($Fe^{2+/3+}$, Zn^{2+}, Mn^{2+} and Cu^{2+})[32,33] and cGAS-STING signalling (Zn^{2+} and Mn^{2+})[34,35]. 'Metalloimmunotherapy' may harness the immune modulatory functions of metal ions for disease treatment. For example, Mg^{2+} increases NKG2D expression and restores the cytotoxicity of natural killer (NK) and T cells for Epstein–Barr virus infection treatment[36]. Potassium (K^+) preserves T cell stemness and increases the persistence and potency of T cells[28]. In particular, recent studies have shown that Mn^{2+} sensitizes the cGAS-STING pathway to double-stranded DNA during DNA virus infection[34] and synergizes with immune checkpoint inhibitors[37], chemotherapy[38], in situ vaccine[39] and photodynamic therapy[40]. However, despite their promise, how to systemically develop an effective metalloimmunotherapy and deliver it in appropriate pharmaceutical forms remains largely unknown.

Here, we have developed a metalloimmunotherapy based on coordination nanomedicine as a new form of cancer immunotherapy (Fig. 1). Briefly, we screened various metal ions for potential synergy with STING agonists and discovered that Mn^{2+} and Co^{2+} could significantly augment type I IFN (IFN-I) activity of STING agonists. As Mn^{2+} is an essential inorganic trace element required for the immune system[34,41] and is used in US Food and Drugs Administration-approved pharmaceuticals[42–44], we focused on the combination of Mn^{2+} and STING agonists. We report here that Mn^{2+} markedly increases the IFN-I activities of STING agonists in multiple human STING haplotypes. We also demonstrate

[1]Department of Pharmaceutical Sciences, University of Michigan, Ann Arbor, MI, USA. [2]Biointerfaces Institute, University of Michigan, Ann Arbor, MI, USA. [3]Department of Periodontics and Oral Medicine, University of Michigan, Ann Arbor, MI, USA. [4]Department of Biomedical Engineering, University of Michigan, Ann Arbor, MI, USA. [5]College of Pharmacy, Chonnam National University, Gwangju, Republic of Korea. [6]Department of Biostatistics and Bioinformatics, Roswell Park Comprehensive Cancer Center, Buffalo, NY, USA. [7]Department of Otolaryngology, University of Michigan, Ann Arbor, MI, USA. [8]Rogel Cancer Center, University of Michigan, Ann Arbor, MI, USA. ✉e-mail: moonjj@umich.edu

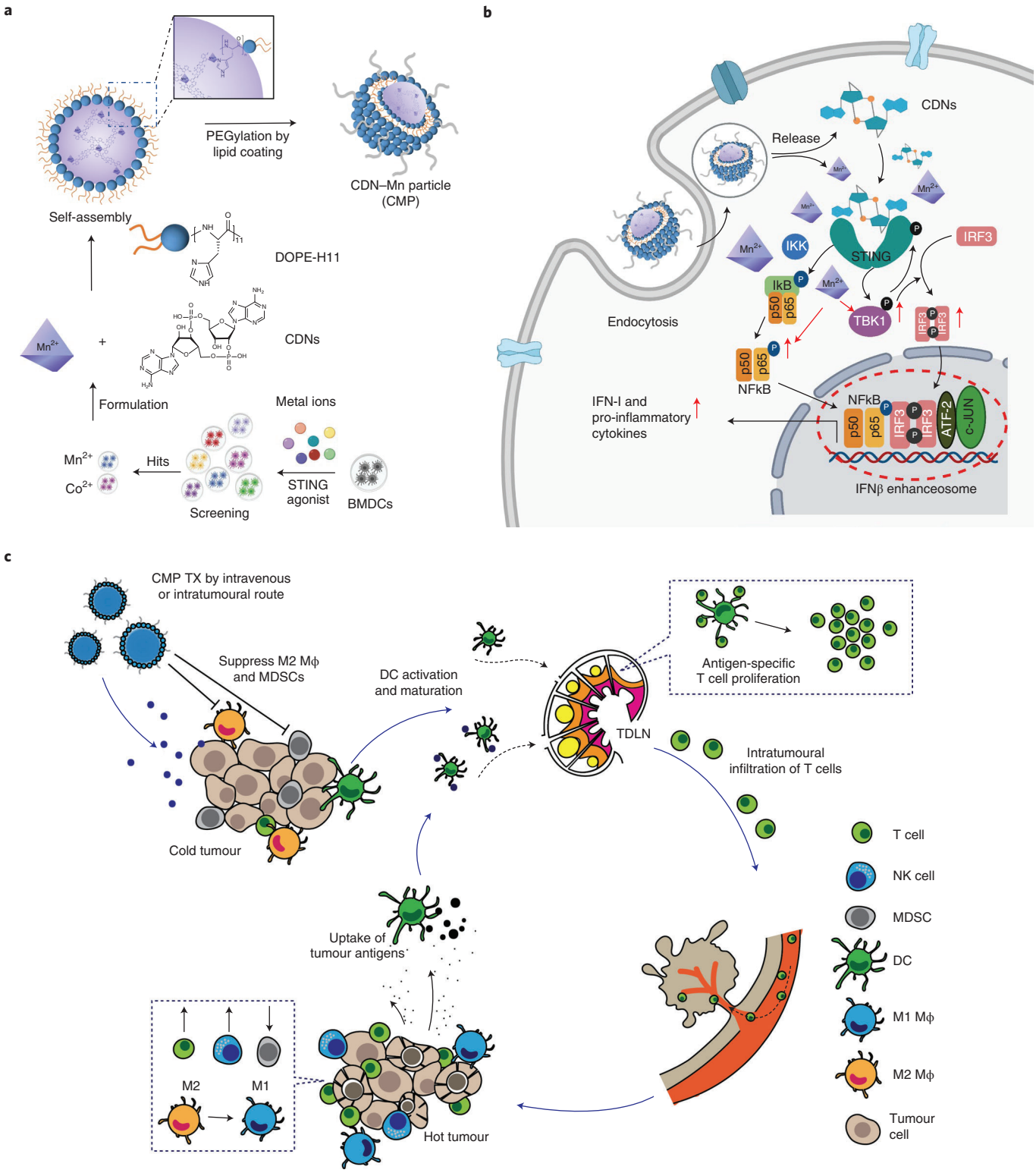

Fig. 1 | Amplifying STING activation with CMPs for cancer metalloimmunotherapy. a, The CMP is composed of CDNs, Mn^{2+}, phospholipid-(histidine)$_{11}$ (DOPE-H11) and a PEG-lipid layer (DOPC:cholesterol:DSPE-PEG5000). Mn^{2+} potentiates the IFN-I activities of STING agonists. Mn^{2+} and CDNs self-assemble into a coordination polymer. The CDN–Mn^{2+} coordination polymer is coated with DOPE-H11 through Mn–histidine coordination to form CDN–Mn@DOPE, followed by PEGylation with a PEG-lipid layer, resulting in the formation of the CMPs. **b**, CMPs boost STING activation: (1) the CMPs promote the cellular uptake of CDNs and Mn^{2+}, and (2) Mn^{2+} augments CDN-induced STING activation by STING-independent TBK1 and p65 phosphorylation, STING-dependent IRF3 phosphorylation and assembly of the IFNβ transcriptional enhanceosome. P, phosphorylation. **c**, CMPs exert potent anti-tumour efficacy after i.t. or i.v. administration. CMPs reverse the immunosuppressive TME while activating T cells, NK cells and DCs. Mϕ, macrophage; TX, treatment. BioRender.com was used to create **a** and **b**.

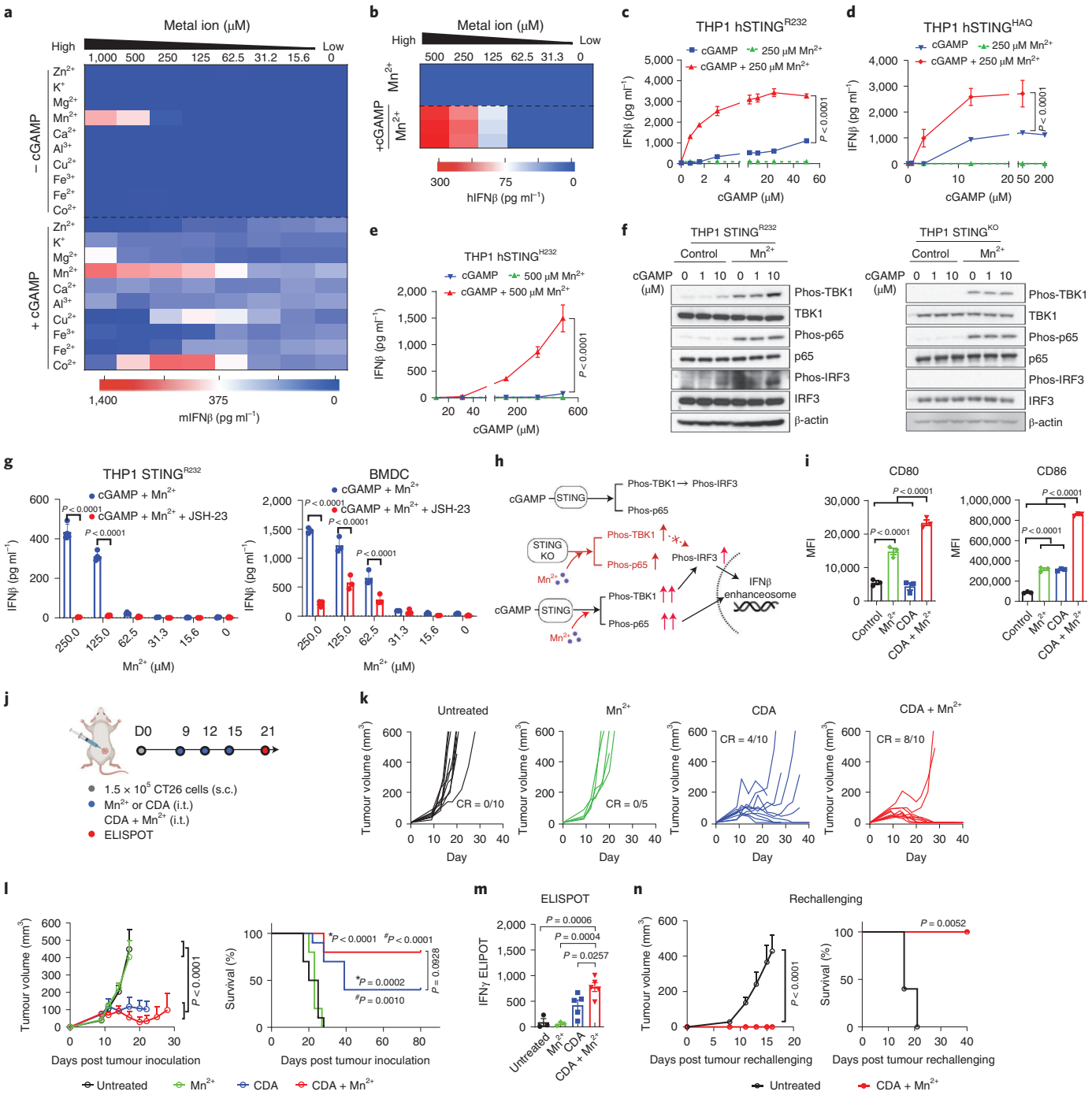

Fig. 2 | Mn^{2+} augments IFN-I activity of STING agonists. a,**b**, BMDCs (**a**) or THP1 (**b**) cells were incubated with various concentrations of metal ions with or without 5 μM cGAMP, and after 24 h, IFNβ secretion was quantified. **c**–**e**, THP1 cells expressing hSTING^{R232} (**c**), hSTING^{HAQ} (**d**) or hSTING^{H232} (**e**) were treated for 24 h with cGAMP with or without Mn^{2+}, followed by quantification of IFNβ production. **f**, THP1 STING^{R232} or THP1 STING^{KO} cells were incubated with increasing concentrations of cGAMP with or without 250 μM Mn^{2+} for 6 h, followed by immunoblotting for marker proteins in the STING-IFN-I pathway. Representative data from two independent experiments with similar results are shown. **g**, Pharmacological inhibition of p65 nucleus translocation inhibits Mn^{2+}-potentiated IFNβ production. **h**, Proposed mechanism of the Mn^{2+}-mediated potentiation of STING agonist by STING-independent TBK1 and p65 phosphorylation and STING-dependent IRF3 phosphorylation. The activation of p65 and IRF3 further facilitates the assembly of the IFNβ transcriptional enhanceosome. KO, knockout. **i**, BMDCs treated with 5 μM CDA, 250 μM Mn^{2+} or their combination for 24 h were analysed for activation by flow cytometry. MFI, mean fluorescence intensity. **j**–**n**, CT26 tumour-bearing BALB/c mice were treated by i.t. administration with 20 μg CDA, 17.5 μg Mn^{2+} or their combination on days 9, 12 and 15 (**j**), mice were monitored for tumour growth (**k**,**l**) and survival (**l**), AH1-specific T cells among PBMCs were assessed by ELISPOT on day 21 (**m**) and survivors from the CDA + Mn^{2+} group were rechallenged with CT26 cells on day 80 (**n**). CR, complete response. The data represent mean ± s.e.m., from a representative experiment of 2–3 independent experiments with $n = 3$–4 (**c**–**e**,**g**,**i**) and $n = 5$–10 (**k**–**n**) biologically independent samples. The data were analysed by one-way analysis of variance (ANOVA; **i**,**m**) or two-way ANOVA (**c**–**e**,**g**,**l**,**n**) with Bonferroni's multiple comparisons test, or log-rank (Mantel–Cox) test (**l**,**n**). *P and #P in **l** denote the statistical significance relative to the untreated or Mn^{2+} group, respectively. Parts **h** and **j** were created with BioRender.com.

that Mn^{2+} self-assembles with CDN STING agonists to form a coordination nanoparticle (CDN–Mn^{2+} particle, CMP) that elicits robust anti-tumour immunity after local or systemic administration (Fig. 1a,b). Using cyclic di-AMP (CDA) as an example, we show that CMP_{CDA} administered through an either i.t. or intravenous (i.v.) route significantly increased STING activation, reversed immunosuppression in the TME and exerted remarkable anti-tumour efficacy (Fig. 1c). Overall, the CMP, a coordination nanomedicine composed of bioactive metal ions and STING agonists, is a promising novel platform for metalloimmunotherapy.

Mn^{2+} potentiates STING agonist activity and IFN-I response

Specifically, we examined the cGAS-STING-IFN-I pathway and screened various nutritional metal ions (for example, Zn^{2+}, K^{+}, Mg^{2+}, Mn^{2+}, Ca^{2+}, Al^{3+}, Cu^{2+}, Fe^{3+}, Fe^{2+} and Co^{2+}) for potentiating STING agonists as a new form of metalloimmunotherapy. To our surprise, adding either Mn^{2+} or Co^{2+} to cGAMP dramatically increased the IFN-1 production in murine bone marrow-derived dendritic cells (BMDCs; Fig. 2a) and in human monocyte-like THP1 cells in a dose-dependent manner (Fig. 2b and Supplementary Fig. 1a). Given the previous examples of Mn^{2+}-based pharmaceuticals[42–44], we further investigated the combination of Mn^{2+} and STING agonists. We examined the impact of Mn^{2+} on human STING (hSTING) haplotypes known to exhibit distinct response profiles to STING agonists. The addition of Mn^{2+} to various concentrations of cGAMP significantly amplified the IFN-I responses in THP1 cells expressing $hSTING^{R232}$, $hSTING^{H232}$ or $hSTING^{HAQ}$, achieving a 77-, 14- and 12-fold dose-sparing effect, respectively (Fig. 2c–e). The allele frequencies of $hSTING^{R232}$, $hSTING^{H232}$ and $hSTING^{HAQ}$ in humans are 57.9, 20.4 and 13.7%, respectively[7]. Even the insensitive $hSTING^{H232}$, which did not respond to as high as 500 μM cGAMP, exhibited a strong IFNβ response when Mn^{2+} was added (Fig. 2e), suggesting that Mn^{2+} offers a widely applicable strategy that covers >90% allele frequency of human STING variants. In addition, Mn^{2+} in doses ranging from 500 μM down to 62.5 μM amplified the IFN-I-inducing activities of other CDN-based STING agonists, including CDA (ref. [45]), ADU-S100 (ref. 7) and 2′3′-cGAM(PS)2 (Rp/Sp)[46], as well as a non-CDN STING agonist, diABZI (ref. [14]; Supplementary Figs. 1b–e and 2a–e). These results indicate that the Mn^{2+}-mediated potentiation of STING agonists is a general phenomenon independent of STING variants and STING agonist structures.

To characterize the mechanism of Mn^{2+}-amplified STING activation, we first performed a thermal shift assay of STING (both $hSTING^{R232}$ and $hSTING^{H232}$) binding to various STING agonists. However, regardless of the STING agonists and STING variants of choice, Mn^{2+} did not increase the binding affinity between STING and STING agonists (Supplementary Fig. 3). Thus, we examined the impact of STING agonist + Mn^{2+} on the downstream of the STING-IFN-I signalling pathway. Maximal transcription of IFN-I genes depends on the formation of an enhanceosome, which contains phosphorylated IRF3 and p65 (refs. [47–49]). Hence, we focused on these two transcription factors. The combination of cGAMP + Mn^{2+} potently enhanced the levels of phosphorylated TBK1, IRF3 and p65 in $hSTING^{R232}$ THP1 cells (Fig. 2f). Interestingly, Mn^{2+} alone without cGAMP still induced phosphorylation of TBK1 and p65 (Fig. 2f). Notably, in STING-knockout THP1 cells and STING-deficient murine BMDCs from Goldenticket mice ($STING^{gt/gt}$), Mn^{2+} triggered STING-independent phosphorylation of TBK1 and p65, but not IRF3 (ref. [50]; Fig. 2f and Supplementary Figs. 4 and 5). In $hSTING^{R232}$ THP1 cells, $hSTING^{H232}$ THP1 cells and murine wild-type (WT) BMDCs, the addition of JSH-23, an inhibitor of p65 nucleus translocation[51], abrogated IFNβ production promoted by cGAMP + Mn^{2+} (Fig. 2g and Supplementary Fig. 5). Taken together, Mn^{2+} shows STING-independent immune activating potential by inducing phosphorylation of TBK1 and p65, which is further augmented and translated to IRF3 phosphorylation in the presence of STING agonists, resulting in amplification of the STING signalling cascade and production of type I IFNs (Fig. 2h).

We evaluated the effects of STING agonist + Mn^{2+} on dendritic cells (DCs). Although CDA or Mn^{2+} promoted BMDC maturation as single agents, the CDA + Mn^{2+} combination significantly upregulated CD80 and CD86 on BMDCs (Fig. 2i and Supplementary Fig. 6). We examined the therapeutic efficacy of CDA + Mn^{2+} in vivo. BALB/c mice were inoculated with CT26 colon carcinoma cells subcutaneously on day 0, and 20 μg CDA, 17.5 μg Mn^{2+} (in 40 μg $MnCl_2$) or their combination was administered intratumourally on days 9, 12 and 15 (Fig. 2j). CDA + Mn^{2+} eradicated CT26 tumours in 80% of mice (Fig. 2k–l). In contrast, CDA monotherapy eliminated tumours in only 40% of mice, and $MnCl_2$ treatment alone showed no benefit (Fig. 2k–l). We assessed $CD8^{+}$ T cell responses against CT26 cells by performing the IFNγ enzyme-linked immune absorbent spot (ELISPOT) assay with peripheral blood mononuclear cells (PBMCs) restimulated with AH1 epitope ($H\text{-}2L^{d}$-restricted SPSYVYHQF, the immunodominant MHC-I minimal epitope of CT26 gp70, ref. [52]). Mice treated with CDA + Mn^{2+} exhibited a significantly elevated antigen-specific T cell response, compared with either CDA or Mn^{2+} monotherapy (Fig. 2m). In addition, 100% of survivors from the CDA + Mn^{2+} treatment group were resistant to CT26 tumour rechallenge performed on day 80 (Fig. 2n). These results show that Mn^{2+} potentiates STING agonist activity and induces robust anti-tumour T cell response with long-term memory.

CDN–Mn^{2+} self-assembled into CMPs amplify STING activation

Despite these promising results, the free admixture of CDNs and Mn^{2+} has a number of limitations, including their poor metabolic stability, cellular permeability as well as potential safety concerns[17]. We sought to address these issues by developing a delivery system that can co-deliver STING agonists and Mn^{2+} and achieve dose sparing with minimal side effects (Fig. 1). We discovered that Mn^{2+} mixed with various CDNs in methanol, including CDA, cyclic di-GMP (CDG) and cGAMP, coordinated their self-assembly into coordination polymers with diameters ranging from nanometres to micrometres (Fig. 3a). We also observed the formation of coordination polymers when CDA was mixed in water with either Mn^{2+} or Zn^{2+}, but not with Ca^{2+}, manganese phosphate or calcium phosphate (Supplementary Fig. 7). Based on the Mn^{2+}-mediated potentiation of the IFN-I response and the fact that STING agonists in clinical trials are mainly derived from CDA[53], we focused on the CDA + Mn^{2+} combination for the remainder of this study. Isothermal titration calorimetry (ITC) analysis indicated that the CDA–Mn^{2+} interaction in methanol fitted a multiple-site binding model with association constants K_{a1} and K_{a2} of 9.367×10^{8} and $1.206 \times 10^{7}\ M^{-1}$, respectively, whereas the CDA–Mn^{2+} interaction in water fitted an independent binding model with a dissociation constant K_D of 1 mM (Supplementary Fig. 8). However, under physiological conditions, the CDA–Mn^{2+} interaction was unstable, leading to rapid dissolution in phosphate-buffered saline (PBS) solution. Thus, to stabilize the CDA–Mn^{2+} coordination polymer, we added dioleoyl-*sn*-glycero-3-phosphoethanolamine-*N*-$(histidine)_{11}$ (DOPE-H11) (Supplementary Fig. 9), which served as an additional coordination ligand and promoted the formation of a hydrophobic core, and is termed CDA–Mn@DOPE. To allow for aqueous suspension, we coated CDA–Mn@DOPE with an outer poly(ethylene glycol) (PEG)-lipid layer by resuspension in a solution mixture of 1,2-dioleoyl-sn-glycero-3-phosphocholine (DOPC):–cholesterol–1,2-distearoyl-sn-glycero-3-phosphoethanolamine (DSPE)-PEG5000 (4:1:1 molar ratio), followed by solvent evaporation and rehydration. The resulting CDA–Mn^{2+} particles, termed CMP_{CDA}, exhibited a uniform spherical morphology with an average

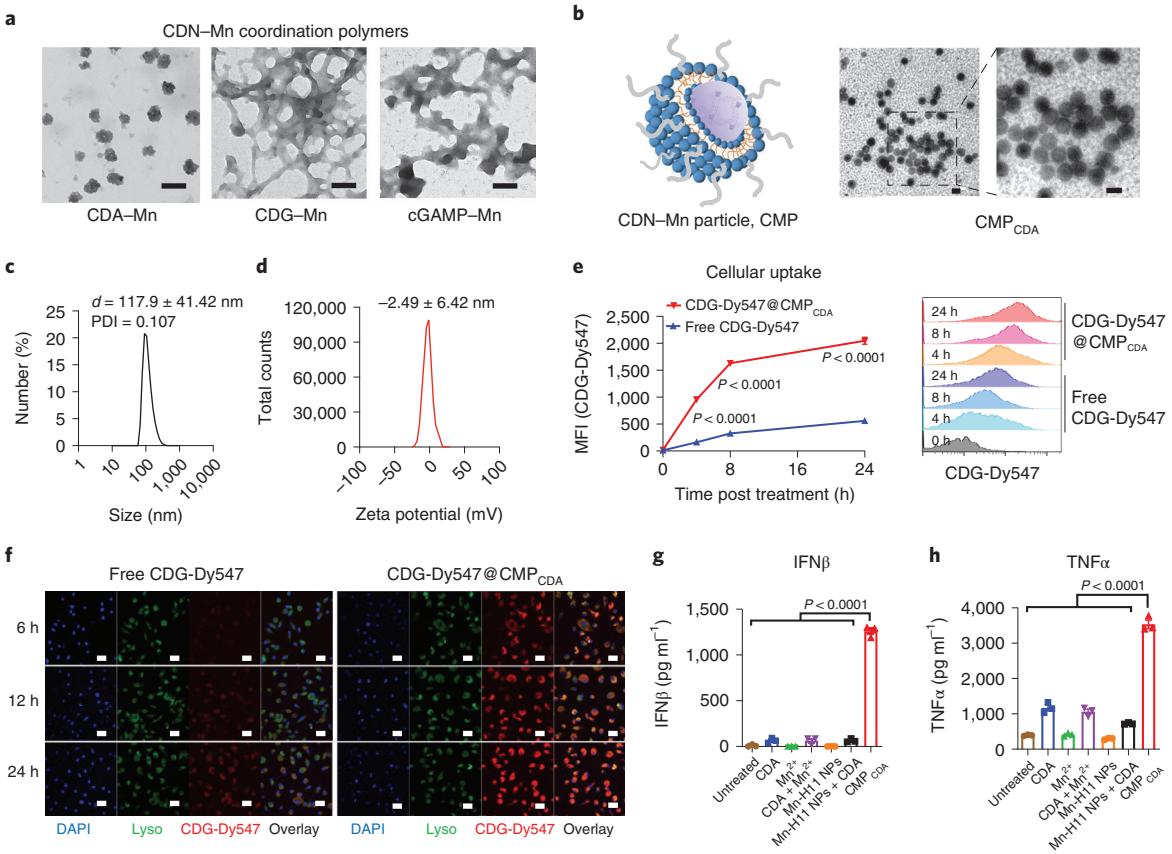

Fig. 3 | CMPs co-delivering Mn^{2+} and STING agonist amplify STING activation. a, Self-assembly behaviour of CDNs and Mn^{2+}. Transmission electron microscopy (TEM) images of CDN–Mn coordination polymers formed by mixing CDA, CDG or cGAMP with Mn^{2+} (10:1, n/n) for 1 h. Scale bars, 100 nm; n/n, molar ratio. **b**, TEM images showing homogeneous CMP_{CDA} formed by coating CDA–Mn coordination polymers with a PEGylated lipid layer. Scale bars, 100 nm. **c**,**d**, Dynamic light scattering (**c**) and zeta potential (**d**) analyses of CMP_{CDA}. **e**,**f**, CMP_{CDA} increased the cellular uptake of STING agonist. BMDCs were incubated with free CDG-Dy547 or CDG-Dy547@CMP_{CDA} for 6, 12 or 24 h, followed by analysis by flow cytometry (**e**) and confocal microscopy (**f**). Scale bars, 10 μm. **g**,**h**, CMP_{CDA} increased STING activation and cytokine production. BMDCs were treated for 24 h with 2.5 μM CDA and/or 15.6 μM Mn^{2+} in free form, blank nanoparticles without CDA (Mn-H11 NPs) or with CDA (Mn-H11 NPs + CDA), or CMP_{CDA}, followed by quantification of IFNβ (**g**) and TNFα (**h**) secretion by the enzyme-linked immunosorbent assay (ELISA). H11, $(histidine)_{11}$. The TEM images in **a** and **b** and the confocal microscopy images in **f** are representative data from two independent experiments with similar results. The data represent mean ± s.e.m. from a representative experiment of two independent experiments with $n = 3$ (**e**,**g**,**h**) biologically independent samples. The data were analysed by one-way ANOVA (**g**,**h**) or two-way ANOVA (**e**) with Bonferroni's multiple comparisons tests.

hydrodynamic diameter (d) of 118 ± 41 nm, a polydispersity index (PDI) of 0.107 and a neutral surface charge (Fig. 3b–d). CDA and Mn^{2+} were efficiently loaded into CMP_{CDA} with loading efficiencies of 39.6 and 25.3% and loading capacities (wt/wt) of 13.2 and 6.72% for CDA and Mn^{2+}, respectively.

We employed CDG-Dy547, a fluorophore-labelled CDN, to track the cellular uptake of STING agonists by BMDCs. Soluble CDG-Dy547 was poorly internalized by the BMDCs (Fig. 3e,f). In stark contrast, CMP_{CDA} carrying CDG-Dy547 exhibited significantly increased cellular uptake, with a 6.3-fold improvement at 4 h ($P < 0.0001$, Fig. 3e). Confocal microscopic images of the BMDCs showed cytosolic localization of the CMPs with gradually reduced overlap with the Lysotracker signal over time (Fig. 3f), suggesting CMP-mediated trafficking of CDN to the cytosol where STING is expressed. CMP_{CDA} increased IFNβ secretion by the BMDCs by >20-fold compared with free CDA, Mn^{2+} or their admixture (Fig. 3g). CMP-mediated co-delivery of CDA and Mn^{2+} was crucial for robust STING activation as blank nanoparticles without CDA (Mn-H11 NPs) or blank nanoparticles admixed with free CDA (Mn-H11 NPs + CDA) induced a weak IFNβ response (Fig. 3g). We also observed similar responses with tumour necrosis factor α (TNFα) secretion (Fig. 3h). Taken together, the CMPs significantly augment the cellular uptake of CDA, STING activation and IFNβ response in vitro.

Local CMP administration eliminates established tumours

Next, we evaluated the therapeutic efficacy of CMPs in vivo. CT26 tumour-bearing BALB/c mice were treated on days 9, 12 and 15 by i.t. administration of CDA and Mn^{2+} in CMPs or soluble formulation (Fig. 4a). Whereas 20 μg CDA and 17.5 μg Mn^{2+} were used in the experiments leading to Fig. 2j–n, here we decreased their doses to 5 μg CDA and 2.5 μg Mn^{2+} to examine the dose-sparing effect of CMP_{CDA}. Intratumoural injection of CMP_{CDA} led to significantly improved immune activation, as shown by elevated levels of IFNβ, TNFα, CXCL10 and CCL5 compared with the free CDA + Mn^{2+} admixture (Fig. 4b). CMP_{CDA} also induced a robust AH1-specific $CD8^+$ T cell response (Fig. 4c and Supplementary Fig. 10). Importantly, CMP_{CDA} eradicated 78% of established tumours, compared with a 30% response rate for the soluble CDA + Mn^{2+} ($P < 0.05$; Fig. 4d,e). In addition, 100% of survivors from the CMP_{CDA} group were resistant to the CT26 tumour rechallenge performed on day 145 (Fig. 4f). Remarkably, even with a minute dose

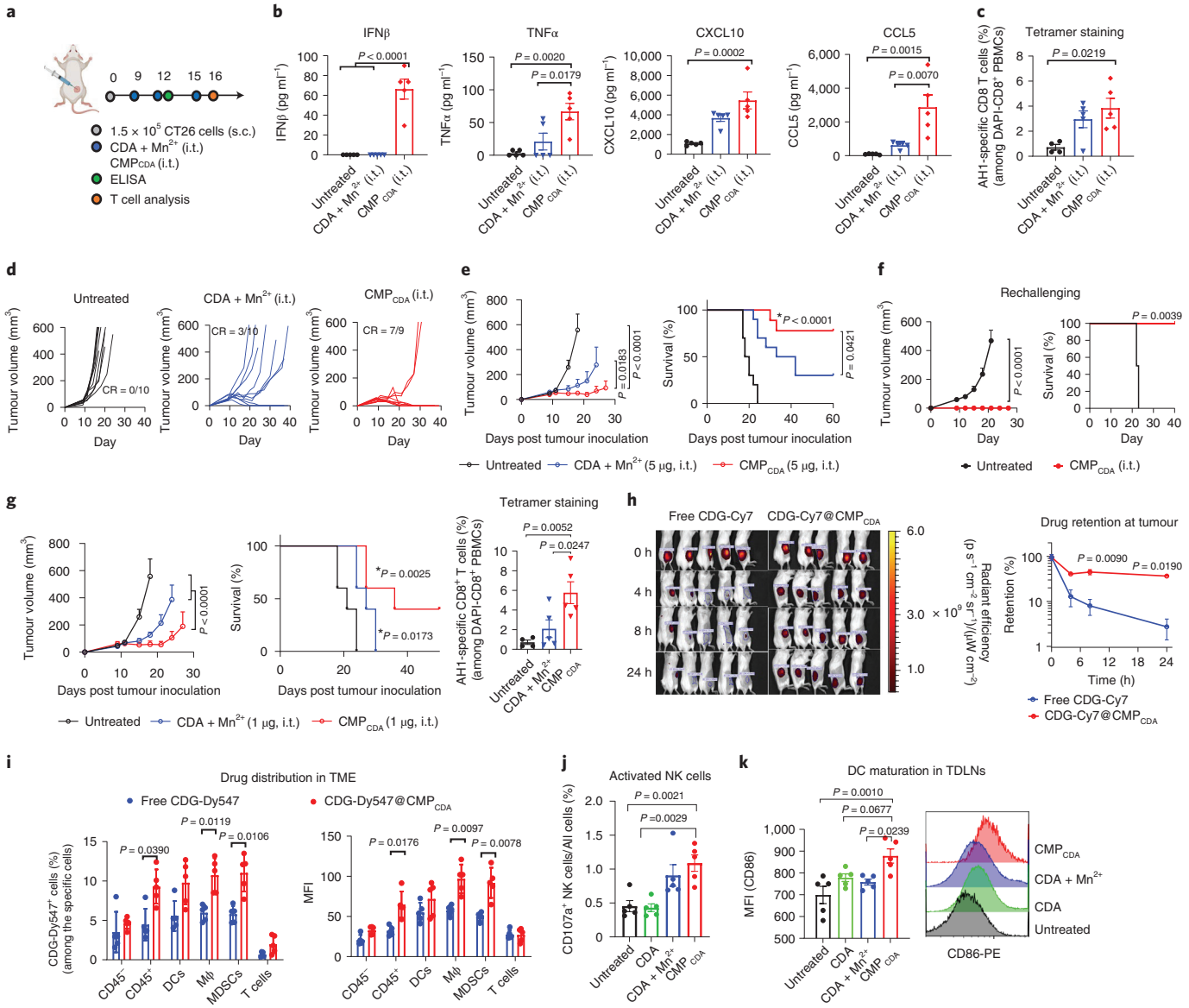

Fig. 4 | Local intratumoural administration of CMP_{CDA} eliminates established tumours. a–f, BALB/c mice were inoculated with 1.5×10^5 CT26 tumour cells in the s.c. flank and treated intratumourally with CDA + Mn^{2+} or CMP_{CDA}, containing 5 μg CDA and 2.5 μg Mn^{2+}, on days 9, 12 and 15 (**a**), serum cytokines were measured by ELISA at 6 h after the second dose (**b**), the antigen-specific T cell response in PBMCs was analysed by AH1 tetramer staining on day 16 (**c**), tumour growth (**d**,**e**) and animal survival (**e**) were monitored over time, and survivors were rechallenged with CT26 tumour cells on day 145 (**f**). **g**, BALB/c mice were inoculated with 1.5×10^5 CT26 tumour cells in the s.c. flank and treated intratumourally with CDA + Mn^{2+} or CMP_{CDA}, containing 1 μg CDA and 0.5 μg Mn^{2+}, on days 9, 12 and 15. Tumour growth and survival were monitored, and the antigen-specific T cell response was analysed on day 16. **h**, CDG-Cy7 either in free or CMP_{CDA} form was administered intratumourally, and retention of the STING agonist within the TME was quantified by in vivo imaging. **i**, CDG-Dy547 either in free or CMP_{CDA} form was administered intratumourally, and the CDG-Dy547 signal among immune cells within the TME was analysed after 6 h by flow cytometry. **j**,**k**, CT26 tumour-bearing mice were treated as in **g** and analysed on day 16 by flow cytometry for the frequency of $CD107a^+$ NK cells within tumours (**j**) and CD86 expression on DCs in TDLNs (**k**). The data represent mean ± s.e.m. from a representative experiment of two independent experiments with $n = 4$–5 (**b**,**c**,**f**–**k**) and $n = 9$–10 (**d**,**e**), analysed by one-way ANOVA (**b**,**c**,**g**,**j**,**k**) or two-way ANOVA (**e**–**h**) with Bonferroni's multiple comparisons test, or two-tailed multiple *t*-tests with Bonferroni–Dunn correction (**i**), or log-rank (Mantel–Cox) test (**e**–**g**). *P in **e** and **g** denotes the statistical significance relative to the untreated group. Part **a** was created with BioRender.com.

of 1 μg CDA and 0.5 μg Mn^{2+}, CMP_{CDA} induced strong immune activation and eliminated established tumours in 40% of mice, compared with a 0% response rate for the soluble CDA + Mn^{2+} (Fig. 4g and Supplementary Fig. 11). We also tested CMP i.t. therapy on untreated, distal tumours in a two-tumour model (Supplementary Fig. 12). As reported previously for the free STING agonist[53], although a high dose of 20 μg CMPs was better at inhibiting primary tumour growth, lower doses of CMPs (either 1 or 5 μg CDA) exerted a robust abscopal effect against distal tumours, significantly outperforming free CDA injections, without any overt body weight change.

Next, we examined how CMP potentiates STING activation. First, we measured the retention and distribution of STING agonists delivered through CMP_{CDA} in the TME. Within 24 h of i.t.

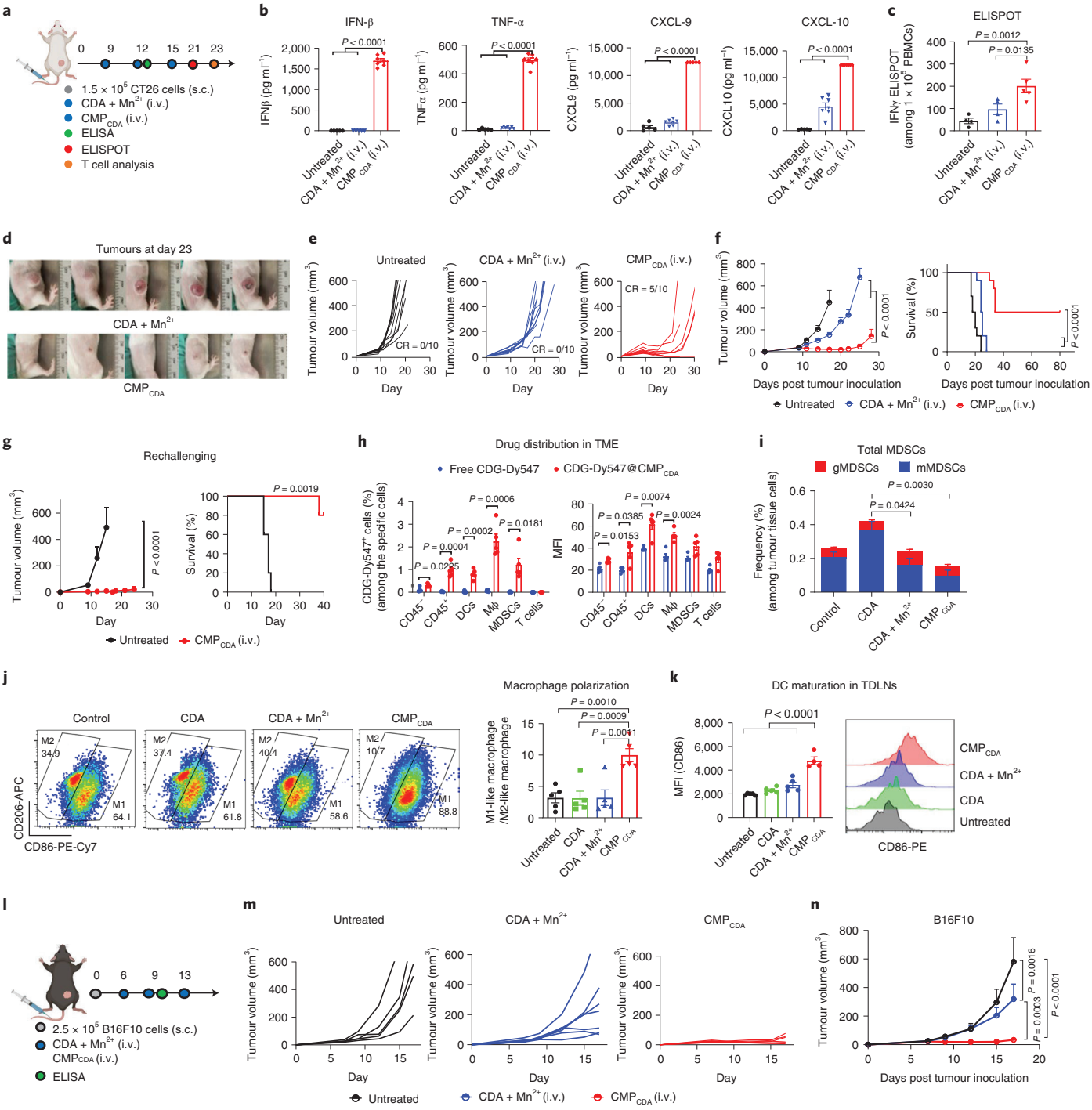

Fig. 5 | Systemic i.v. administration of CMP_{CDA} eliminates established tumours. a–g, Therapeutic effects of CMP_{CDA} on CT26 tumours after i.v. administration: CT26 tumour-bearing BALB/c mice were treated intravenously with CDA + Mn^{2+} or CMP_{CDA}, containing 20 μg CDA and 10 μg Mn^{2+}, on days 9, 12 and 15 (**a**), serum cytokines were measured by ELISA 6 h after the second dose (**b**), the antigen-specific T cell response was analysed on day 21 by restimulating PBMCs with AH1 peptide, followed by an IFNγ ELISPOT assay (**c**), tumour growth (**d**–**f**) and animal survival (**f**) were monitored over time, and survivors rechallenged with CT26 tumour cells on day 145 were monitored for tumour growth and survival (**g**). **h**, CDG-Dy547 either in free form or CMP_{CDA} was administered intravenously and the CDG-Dy547 signal among immune cells within the TME was analysed after 24 h by flow cytometry. **i**–**k**, CT26 tumour-bearing mice were treated as in **a** and TME was analysed on day 17 by flow cytometry for the frequency of granulocytic and monocytic MDSCs (gMDSC and mMDSC, respectively; **i**), M1- and M2-like macrophages within the TME (representative scatter plots are shown; **j**) and CD86 expression on DCs in TDLNs (**k**). **l**–**n**, Therapeutic effects of CMP_{CDA} on B16F10 tumours after i.v. administration: B16F10 tumour-bearing C57BL/6 mice were treated intravenously with CDA + Mn^{2+} or CMP_{CDA}, containing 20 μg CDA and 10 μg Mn^{2+}, on days 6, 9 and 13 (**l**), and individual tumour growth (**m**) and average tumor size (**n**) were monitored over time. The data represent mean ± s.e.m. from a representative experiment of two independent experiments with $n = 5$ (**b**,**c**,**g**–**k**), $n = 5$–7 (**m**,**n**) and $n = 10$ (**e**,**f**). The data were analysed by one-way ANOVA (**b**,**c**,**j**,**k**) or two-way ANOVA (**f**,**g**,**i**,**n**) with Bonferroni's multiple comparisons test, or two-tailed multiple *t*-tests with Bonferroni–Dunn correction (**h**), or log-rank (Mantel–Cox) test (**f**,**g**). Parts **a** and **l** were created with BioRender.com.

administration, free CDG-Cy7 was rapidly cleared from the TME, whereas a 13.4-fold higher CDG-Cy7 signal was detected for the CDG-Cy7@CMP_{CDA} group (Fig. 4h). CDG-Dy547@CMP_{CDA} substantially improved the cellular uptake of CDN by $CD11c^+$ DCs, $F4/80^+$ macrophages and $Ly6C^+$ myeloid-derived suppressor cells (MDSCs; Fig. 4i and Supplementary Figs. 13 and 14), but not among $CD45^-$ tumour cells and $CD3^+$ T cells. We also analysed the changes in the activation status of immune cells after CMP_{CDA} treatment. Compared with free CDA with or without Mn^{2+}, CMP_{CDA} treatment promoted activation of intratumoural NK cells (Fig. 4j and Supplementary Fig. 15) and DCs in tumour-draining lymph nodes (TDLNs; Fig. 4k). Taken together, CMP_{CDA} efficiently modulates the TME, in part by promoting tissue retention of STING agonists and their uptake by local immune cells, leading to Mn^{2+}-mediated potentiation of STING agonists and anti-tumour immune response.

Systemic CMP therapy exerts potent anti-tumour effects

Due to rapid enzymatic degradation and poor drug-like properties, most STING agonists in clinical trials are administered directly into tumours; however, i.t. treatment is not applicable for metastatic tumours. To address this issue, we evaluated the therapeutic effect of CMPs after i.v. administration. CT26 tumour-bearing BABL/c mice were treated intravenously on days 9, 12 and 15 with 20 μg CDA and 10 μg Mn^{2+} either in CMP_{CDA} or soluble form (Fig. 5a). Compared with the soluble control group, CMP_{CDA} promoted accumulation of Mn^{2+} and CDN in the TME (Supplementary Fig. 16) and significantly increased the serum levels of IFNβ, TNFα, CXCL9 and CXCL10 (Fig. 5b). As shown by the IFNγ ELISPOT assay performed on PBMCs, CMP_{CDA} administered intravenously significantly enhanced the AH1-specific $CD8^+$ T cell response compared with the soluble CDA + Mn^{2+} control (Fig. 5c and Supplementary Fig. 17). Importantly, CMP_{CDA} administered intravenously significantly decreased CT26 tumour growth and eliminated established tumours in 50% of mice ($P < 0.0001$; Fig. 5d–f), whereas treatment with soluble CDA + Mn^{2+} had a 0% response rate. Notably, even increasing the dose of free CDA i.v. therapy to 100 μg could not control tumour growth, whereas 20 μg CMP_{CDA} i.v. therapy regressed established tumours (Supplementary Fig. 18). Flow cytometric analysis performed on day 23 showed that CMP_{CDA} i.v. therapy significantly expanded $CD8^+$ T cell subsets with $CD44^+CD62L^+$ central memory and $CD44^+CD62L^-$ effector memory phenotypes (Supplementary Fig. 19). The survivors from the CMP_{CDA} treatment group were largely resistant to CT26 tumour rechallenge performed on day 145 (Fig. 5g). CMP_{CDA} i.v. therapy significantly increased the drug uptake by intratumoural $CD45^+$ immune cells, especially $F4/80^+$ macrophages and $Ly6C^+$ MDSCs (Fig. 5h and Supplementary Figs. 13 and 20). TME analysis revealed that CMP_{CDA} i.v. therapy significantly reduced intratumoural MDSCs and promoted M2-to-M1 repolarization of intratumoural macrophages (Fig. 5i,j and Supplementary Fig. 15), while also inducing robust DC maturation in TDLNs (Fig. 5k). We also validated our results in a second tumour model. In C57BL/6 mice bearing B16F10 melanoma, CMP_{CDA} i.v. therapy exerted significantly enhanced therapeutic efficacy compared with the CDA + Mn^{2+} mixture ($P < 0.001$; Fig. 5l–n and Supplementary Fig. 21). Overall, CMP_{CDA} administered intravenously induces robust anti-tumour immune responses and exhibits potent anti-tumour efficacy.

Benchmarking and validation in multiple tumour models

To further evaluate the potency of CMPs, we performed head-to-head comparison studies between CMP_{CDA} and other STING-activating formulations. C57BL/6 mice were inoculated in the subcutaneous (s.c.) flank with 3×10^5 B16F10 tumours cells, and we administered three doses of CMP_{CDA} at 3-day intervals by either the i.t. route, when the average tumour volume reached $153 \pm 17\ mm^3$ (Fig. 6a–e), or by the i.v. route, when the average tumour volume reached $63 \pm 7\ mm^3$. (Fig. 6f–j). We compared CMP_{CDA} with the equivalent dosage of four other STING-activating therapeutics, namely CDA-loaded liposomes[18], the CZP particle system formed by replacing Mn^{2+} with Zn^{2+} in CMPs (Supplementary Fig. 7), ADU-S100, a leading CDN STING agonist tested in clinical trials[7], and diABZI, a leading non-CDN STING agonist (used as an i.v. formulation, currently in clinical trials[14]). After i.t. therapy, CMP_{CDA} significantly delayed tumour growth, eliminated B16F10 tumours in 30% of animals and prolonged animal survival, whereas other control groups (except for diABZI) showed significantly reduced anti-tumour effects (Fig. 6a–e). Importantly, in the setting of i.v. therapy, CMP_{CDA} also exerted remarkable anti-tumour efficacy, slowing the tumour growth and prolonging animal survival with a 20% complete response (CR) rate (Fig. 6f–j). In stark contrast, all other control groups (including diABZI) had only minor anti-tumour effects in this difficult-to-treat tumour model. Interestingly, even though the CMPs and diABZI generated comparable anti-tumour responses after i.t. therapy, the CMPs significantly outperformed diABZI after i.v. injection (Fig. 6f–j). Moreover, the superiority of CMPs over both CZPs and CDA liposomes demonstrates the indispensable role of Mn^{2+}-mediated potentiation of STING agonists as well as the advantages of our coordination-based STING agonist delivery system.

Lastly, we examined the therapeutic efficacy of CMP in a novel tobacco carcinogen-associated syngeneic squamous cell carcinoma model that is completely refractory to high doses of immune checkpoint blocker (ICB) therapy (Fig. 6k–p and Supplementary Fig. 22). Epithelial malignancies, such as the squamous cell carcinomas of the head and neck, only show a modest response to immunotherapy, typically <15% in the clinics[54]. To model a cold epithelial malignancy, C57BL/6J mice were given 4-nitroquinoline 1-oxide

Fig. 6 | Robust therapeutic effect of CMP_{CDA} in multiple tumour models. a–e, The therapeutic effect of CMP_{CDA} administered intratumourally was compared with other CDA formulations and other STING agonists in an established B16F10 tumour model: tumour-bearing C57BL/6 mice were treated with CMP_{CDA}, CDA–Zn particles (CZP_{CDA}), CDA liposomes, ADU-S100 or diABZI (all i.t., 5 μg doses of STING agonists) at the indicated time points (**a**), individual tumour growth (**b**), representative photographs of tumours (**c**), average tumour growth (**d**) and survival (**e**). **f–j**, The therapeutic effect of CMP_{CDA} administered intravenously was also compared with other CDA formulations and other STING agonists in an established B16F10 tumour model: tumour-bearing C57BL/6 mice were treated intravenously with the indicated regimens (all 20 μg doses; **f**), individual tumour growth (**g**), representative photographs of tumours (**h**), average tumour growth (**i**) and survival (**j**). **k–m**, Therapeutic effect of CMP_{CDA} in an ICB-resistant tobacco-associated tumour model (NOOC1): NOOC1 single-cell clones were isolated from the visible oral squamous cell carcinoma lesions of C57BL/6J mice treated with 4NQO-containing drinking water for 16 weeks (**k**), mutational signatures indicate NOOC1 tumours with high fidelity to human cancers (**l**) and mutational profiles of NOOC1 and other 4NQO-induced murine squamous cell carcinoma cell lines (4MOSCs; **m**). **n–p**, NOOC1 tumour-bearing C57BL/6 mice were treated with CDA in CMP_{CDA} or free form by the i.t. (5 μg dose) or i.v. route (20 μg dose) on days 9, 12, 16 and 20 post tumour inoculation: individual tumour growth (**n**), representative photographs of tumours (**o**) and average tumour growth and survival (**p**). The data represent mean ± s.e.m. from a representative experiment of two independent experiments with $n = 4$–10 (**d**,**e**,**i**,**j**) and $n = 7$–8 (**n**–**p**). The data were analysed by two-way ANOVA (**d**,**i**,**p**) with Bonferroni multiple comparisons post-test. The survival in **e**, **j** and **p** was analysed by Kaplan–Meier survival analysis with the log-rank (Mantel–Cox) test. *P and #P in **p** denote the statistical significance relative to the untreated and CDA groups, respectively. Parts **a**, **f** and **k** were created with BioRender.com.

(4NQO)-containing (50 μg ml^{-1}) drinking water for 16 weeks, and visible oral squamous cell carcinoma lesions were isolated to produce single-cell clones, which were then screened in vitro and in vivo. We identified a cell clone (4-NQO-induced oral cancer 1, NOOC1) that stably produced tumours when implanted in syngeneic C57BL/6J hosts (Fig. 6k). Whole exome sequencing revealed

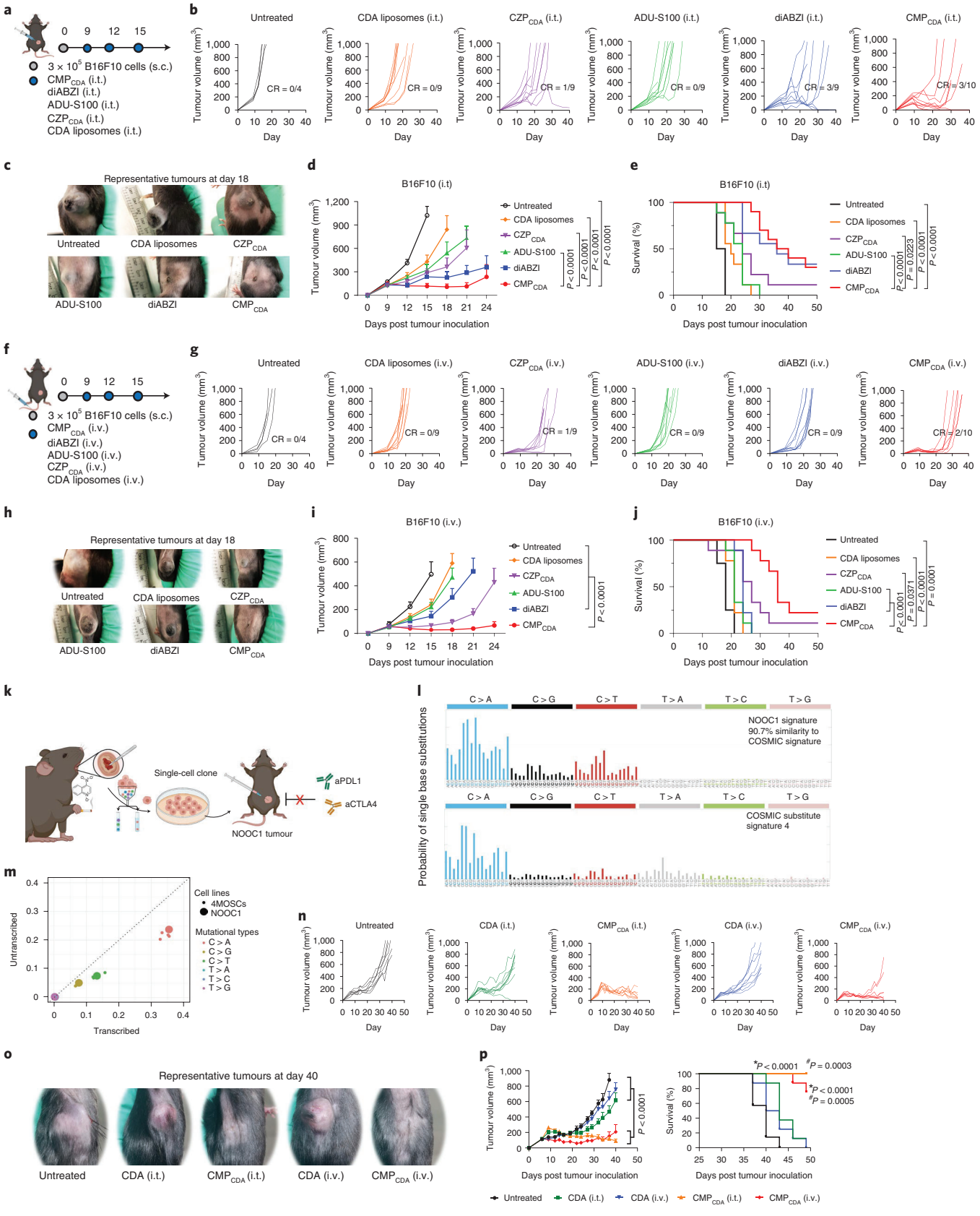

that the mutational signatures of NOOC1 bore 90.7% similarity to the Catalogue of Somatic Mutation In Cancer (COSMIC) signature 4, which is driven by smoking-associated mutations in human cancers (Fig. 6l). The mutation profile of NOOC1 was highly similar to that of 4MOSCs, a recently reported 4-NQO-induced cell line, thus validating its tobacco association (Fig. 6l,m). Notably, NOOC1 was refractory to high doses (six doses of 200 μg) of ICB therapy, including anti-PD-L1 and anti-CTLA4 (Supplementary Fig. 22). To evaluate CMPs in this ICB-resistant epithelial malignancy model, mice were inoculated with 2×10^6 NOOC1 tumour cells, and when the average tumour volume reached >100 mm^3, animals were treated on days 9, 12, 16 and 20 with CMP_{CDA} or free CDA. We employed the equivalent CDA dose of 5 μg for i.t. therapy and 20 μg for i.v. therapy. NOOC1 was also refractory to free CDA treatments, regardless of the administration routes. In stark contrast, both CMP i.t. and i.v. therapy exerted robust anti-tumour efficacy, regressing established NOOC1 tumours ($P<0.0001$) and extending animal survival ($P<0.001$; Fig. 6n–p).

Notably, each injection dose of Mn^{2+} in CMP_{CDA} employed in our i.t. (Fig. 4) and i.v. (Fig. 5) treatment studies was 2.5 and 10 μg (0.13 and 0.5 mg kg^{-1}), respectively. For comparison, the median lethal dose of $MnCl_2$ in mice is 1,715 mg kg^{-1} (ref. [55]), and average adults on typical Western diets consume up to 10 mg of manganese per day[56]. CMP_{CDA} i.v. therapy transiently increased the serum levels of IFNβ, TNFα and IL-6, peaking at 6 h (Supplementary Fig. 23), while inducing a 13.5% maximum body weight loss; however, the animals quickly recovered within 3 days, and multiple treatments of CMP_{CDA} or CDA + Mn^{2+} mixture were generally well-tolerated, as indicated by the serum chemistry and neurotoxicity marker (Supplementary Figs. 24 and 25). In addition, histological analysis of major organs by a pathologist in a blinded manner showed no abnormal histological conditions (Supplementary Fig. 26).

Conclusions

In summary, we have developed a self-assembled coordination nanomedicine based on Mn^{2+} and CDN-based STING agonists. CMPs represent a major technological advancement to amplify the potency of STING agonists. The combination of Mn^{2+} and STING agonists dramatically augmented STING activation (Fig. 2). CMPs effectively delivered Mn^{2+} and STING agonists, and amplified the IFN-I responses (Figs. 3–6 and Supplementary Fig. 16). CMPs administered intratumourally produced strong anti-tumour efficacy, achieving drug dose-sparing with minimal side effects (Figs. 4 and 6 and Supplementary Figs. 11, 12 and 24–26). Moreover, systemic treatments with CMPs exerted remarkable therapeutic efficacy in multiple difficult-to-treat murine tumour models (Figs. 5 and 6 and Supplementary Fig. 18). Our work presents the concept of 'metalloimmunotherapy' and demonstrates, for the first time, the powerful potential of nanomedicine-based cancer metalloimmunotherapy. As nutritional metal ions play crucial roles in various immune processes, metalloimmunotherapy may be broadly applicable to other immune-related diseases.

Online content

Any methods, additional references, Nature Research reporting summaries, source data, extended data, supplementary information, acknowledgements, peer review information; details of author contributions and competing interests; and statements of data and code availability are available at https://doi.org/10.1038/s41565-021-00962-9.

Received: 15 September 2020; Accepted: 23 July 2021;
Published online: 30 September 2021

References

1. Couzin-Frankel, J. Cancer immunotherapy. *Science* **342**, 1432–1433 (2013).
2. Gubin, M. M. et al. Checkpoint blockade cancer immunotherapy targets tumour-specific mutant antigens. *Nature* **515**, 577–581 (2014).
3. Lee, D. W. et al. T cells expressing CD19 chimeric antigen receptors for acute lymphoblastic leukaemia in children and young adults: a phase 1 dose-escalation trial. *Lancet* **385**, 517–528 (2015).
4. Syn, N. L., Teng, M. W., Mok, T. S. & Soo, R. A. De-novo and acquired resistance to immune checkpoint targeting. *Lancet Oncol.* **18**, e731–e741 (2017).
5. Duan, Q., Zhang, H., Zheng, J. & Zhang, L. Turning cold into hot: firing up the tumor microenvironment. *Trends Cancer* **6**, 605–618 (2020).
6. Sun, L., Wu, J., Du, F., Chen, X. & Chen, Z. J. Cyclic GMP-AMP synthase is a cytosolic DNA sensor that activates the type I interferon pathway. *Science* **339**, 786–791 (2013).
7. Corrales, L. et al. Direct activation of STING in the tumor microenvironment leads to potent and systemic tumor regression and immunity. *Cell Rep.* **11**, 1018–1030 (2015).
8. Flood, B. A., Higgs, E. F., Li, S., Luke, J. J. & Gajewski, T. F. STING pathway agonism as a cancer therapeutic. *Immunol. Rev.* **290**, 24–38 (2019).
9. Shae, D. et al. Endosomolytic polymersomes increase the activity of cyclic dinucleotide STING agonists to enhance cancer immunotherapy. *Nat. Nanotechnol.* **14**, 269–278 (2019).
10. Schadt, L. et al. Cancer-cell-intrinsic cGAS expression mediates tumor immunogenicity. *Cell Rep.* **29**, 1236–1248 (2019).
11. Nicolai, C. J. et al. NK cells mediate clearance of $CD8^+$ T cell-resistant tumors in response to STING agonists. *Sci Immunol.* https://doi.org/10.1126/sciimmunol.aaz2738 (2020).
12. Harrington, K. J. et al. Preliminary results of the first-in-human study of MK-1454, an agonist of stimulator of interferon genes (STING), as monotherapy or in combination with Pembrolizumab (Pembro) in patients with advanced solid tumors or lymphomas. In *The European Society for Medical Oncology (ESCO) 2018 Congress* Abstract 5475 (2018).
13. Meric-Bernstam, F. et al. Phase Ib study of MIW815 (ADU-S100) in combination with spartalizumab (PDR001) in patients (pts) with advanced/metastatic solid tumors or lymphomas. *J. Clin. Oncol.* **37**, 2507 (2019).
14. Ramanjulu, J. M. et al. Design of amidobenzimidazole STING receptor agonists with systemic activity. *Nature* **564**, 439–443 (2018).
15. Chin, E. N. et al. Antitumor activity of a systemic STING-activating non-nucleotide cGAMP mimetic. *Science* **369**, 993–999 (2020).
16. Pan, B. S. et al. An orally available non-nucleotide STING agonist with antitumor activity. *Science* https://doi.org/10.1126/science.aba6098 (2020)
17. Gajewski, T. F. & Higgs, E. F. Immunotherapy with a sting. *Science* **369**, 921–922 (2020).
18. Koshy, S. T., Cheung, A. S., Gu, L., Graveline, A. R. & Mooney, D. J. Liposomal delivery enhances immune activation by STING agonists for cancer immunotherapy. *Adv. Biosyst.* https://doi.org/10.1002/adbi.201600013 (2017).
19. Tan, Y. S. et al. Mitigating SOX2-potentiated immune escape of head and neck squamous cell carcinoma with a STING-inducing nanosatellite vaccine. *Clin. Cancer Res.* **24**, 4242–4255 (2018).
20. Liu, Y. et al. An inhalable nanoparticulate STING agonist synergizes with radiotherapy to confer long-term control of lung metastases. *Nat. Commun.* **10**, 5108 (2019).
21. He, Y. et al. Self-assembled cGAMP-STINGΔTM signaling complex as a bioinspired platform for cGAMP delivery. *Sci. Adv.* **6**, eaba7589 (2020).
22. Li, S. et al. Prolonged activation of innate immune pathways by a polyvalent STING agonist. *Nat. Biomed. Eng.* https://doi.org/10.1038/s41551-020-00675-9 (2021).
23. Chaigne-Delalande, B. & Lenardo, M. J. Divalent cation signaling in immune cells. *Trends Immunol.* **35**, 332–344 (2014).
24. Wang, C., Zhang, R., Wei, X., Lv, M. & Jiang, Z. Metalloimmunology: the metal ion-controlled immunity. *Adv. Immunol.* **145**, 187–241 (2020).
25. Macian, F. NFAT proteins: key regulators of T-cell development and function. *Nat. Rev. Immunol.* **5**, 472–484 (2005).
26. Shi, X. et al. Ca^{2+} regulates T-cell receptor activation by modulating the charge property of lipids. *Nature* **493**, 111–115 (2013).
27. Chandy, K. G. & Norton, R. S. Immunology: channelling potassium to fight cancer. *Nature* **537**, 497–499 (2016).
28. Vodnala, S. K. et al. T cell stemness and dysfunction in tumors are triggered by a common mechanism. *Science* https://doi.org/10.1126/science.aau0135 (2019).
29. Munoz-Planillo, R. et al. K^+ efflux is the common trigger of NLRP3 inflammasome activation by bacterial toxins and particulate matter. *Immunity* **38**, 1142–1153 (2013).
30. Rossol, M. et al. Extracellular Ca^{2+} is a danger signal activating the NLRP3 inflammasome through G protein-coupled calcium sensing receptors. *Nat. Commun.* **3**, 1329 (2012).
31. Scambler, T. et al. ENaC-mediated sodium influx exacerbates NLRP3-dependent inflammation in cystic fibrosis. *Elife* https://doi.org/10.7554/eLife.49248 (2019)

32. Hood, M. I. & Skaar, E. P. Nutritional immunity: transition metals at the pathogen–host interface. *Nat. Rev. Microbiol.* **10**, 525–537 (2012).
33. Bessman, N. J. et al. Dendritic cell-derived hepcidin sequesters iron from the microbiota to promote mucosal healing. *Science* **368**, 186–189 (2020).
34. Wang, C. et al. Manganese increases the sensitivity of the cGAS-STING pathway for double-stranded DNA and is required for the host defense against DNA viruses. *Immunity* **48**, 675–687 (2018).
35. Du, M. & Chen, Z. J. DNA-induced liquid phase condensation of cGAS activates innate immune signaling. *Science* **361**, 704–709 (2018).
36. Chaigne-Delalande, B. et al. Mg^{2+} regulates cytotoxic functions of NK and CD8 T cells in chronic EBV infection through NKG2D. *Science* **341**, 186–191 (2013).
37. Lv, M. et al. Manganese is critical for antitumor immune responses via cGAS-STING and improves the efficacy of clinical immunotherapy. *Cell Res.* **30**, 966–979 (2020).
38. Hou, L. et al. Manganese-based nanoactivator optimizes cancer immunotherapy via enhancing innate immunity. *ACS Nano* **14**, 3927–3940 (2020).
39. Chen, C. et al. Cytosolic delivery of thiolated Mn-cGAMP nanovaccine to enhance the antitumor immune responses. *Small* **17**, e2006970 (2021).
40. Yang, X. et al. Converting primary tumor towards an in situ STING-activating vaccine via a biomimetic nanoplatform against recurrent and metastatic tumors. *Nano Today* **38**, 101109 (2021).
41. Aschner, J. L. & Aschner, M. Nutritional aspects of manganese homeostasis. *Mol. Aspects Med.* **26**, 353–362 (2005).
42. Wang, C. Mangafodipir trisodium (MnDPDP)-enhanced magnetic resonance imaging of the liver and pancreas. *Acta Radiol. Suppl.* **415**, 1–31 (1998).
43. Takagi, Y. et al. Evaluation of indexes of in vivo manganese status and the optimal intravenous dose for adult patients undergoing home parenteral nutrition. *Am. J. Clin. Nutr.* **75**, 112–118 (2002).
44. Pan, D., Schmieder, A. H., Wickline, S. A. & Lanza, G. M. Manganese-based MRI contrast agents: past, present and future. *Tetrahedron* **67**, 8431–8444 (2011).
45. Jin, L. et al. MPYS is required for IFN response factor 3 activation and type I IFN production in the response of cultured phagocytes to bacterial second messengers cyclic-di-AMP and cyclic-di-GMP. *J. Immunol.* **187**, 2595–2601 (2011).
46. Li, L. et al. Hydrolysis of 2′3′-cGAMP by ENPP1 and design of nonhydrolyzable analogs. *Nat. Chem. Biol.* **10**, 1043–1048 (2014).
47. Thanos, D. & Maniatis, T. Virus induction of human IFNβ gene expression requires the assembly of an enhanceosome. *Cell* **83**, 1091–1100 (1995).
48. Wang, J. et al. NF-κB RelA subunit is crucial for early IFN-β expression and resistance to RNA virus replication. *J. Immunol.* **185**, 1720–1729 (2010).
49. Ting, J. P., Duncan, J. A. & Lei, Y. How the noninflammasome NLRs function in the innate immune system. *Science* **327**, 286–290 (2010).
50. Liu, S. et al. Phosphorylation of innate immune adaptor proteins MAVS, STING, and TRIF induces IRF3 activation. *Science* **347**, aaa2630 (2015).
51. Shin, H. M. et al. Inhibitory action of novel aromatic diamine compound on lipopolysaccharide-induced nuclear translocation of NF-κB without affecting IκB degradation. *FEBS Lett.* **571**, 50–54 (2004).
52. Kuai, R. et al. Elimination of established tumors with nanodisc-based combination chemoimmunotherapy. *Sci. Adv.* **4**, eaao1736 (2018).
53. Sivick, K. E. et al. Magnitude of therapeutic STING activation determines $CD8^+$ T cell-mediated anti-tumor immunity. *Cell Rep.* **25**, 3074–3085 (2018).
54. Luo, X. et al. HPV16 drives cancer immune escape via NLRX1-mediated degradation of STING. *J. Clin. Invest.* **130**, 1635–1652 (2020).
55. Lewis, R. & Tatken, R. *Registry of Toxic Effects of Chemical Substances* Vol. 1 (US Department of Health and Human Services, National Institute for Occupational Safety and Health, 1980).
56. Greger, J. L. Nutrition versus toxicology of manganese in humans: evaluation of potential biomarkers. *Neurotoxicology* **20**, 205–212 (1999).
57. Lutz, M. B. et al. An advanced culture method for generating large quantities of highly pure dendritic cells from mouse bone marrow. *J. Immunol. Methods* **223**, 77–92 (1999).
58. Liu, D., Poon, C., Lu, K., He, C. & Lin, W. Self-assembled nanoscale coordination polymers with trigger release properties for effective anticancer therapy. *Nat. Commun.* **5**, 4182 (2014).
59. Liu, J. et al. Light-controlled drug release from singlet-oxygen sensitive nanoscale coordination polymers enabling cancer combination therapy. *Biomaterials* **146**, 40–48 (2017).
60. Yang, Y. et al. One-pot synthesis of pH-responsive charge-switchable PEGylated nanoscale coordination polymers for improved cancer therapy. *Biomaterials* **156**, 121–133 (2018).
61. Kuai, R. et al. Subcutaneous nanodisc vaccination with neoantigens for combination cancer immunotherapy. *Bioconjug. Chem.* **29**, 771–775 (2018).

Materials and methods

Assessing metal ions for modulation of IFN-I response of STING agonists in vitro. Mouse BMDCs were isolated and cultured as reported previously[57]. Human monocyte cell line THP1 cells expressing hSTING^{HAQ} were purchased from ATCC and cultured according to ATCC's instruction. THP1 cells expressing hSTING^{R232} (WT) and hSTING^{H232} (REF, reference) were purchased from Invivogen and cultured according to Invivogen's instruction. To screen for metal ions for modulating the IFN-I response of STING agonists, we seeded 1×10^5 BMDCs or THP1 cells per well in 96-well plates, and metal ions (for example, $ZnCl_2$, KCl, $MgCl_2$, $MnCl_2$, $CaCl_2$, $Al_2(SO_4)_3$, $CuCl_2$, $FeCl_2$, $FeCl_3$ and $CoCl_2$; Sigma-Aldrich) at various concentrations in the range 0–500 μM were added with or without 5 μM cGAMP (Invivogen). After 24 h incubation at 37 °C under 5% CO_2, the supernatants were collected for IFNβ ELISA assay (R&D). To evaluate the effect of $MnCl_2$ on the IFN-I response of STING agonists in various human STING variants, the indicated concentrations of $MnCl_2$ and STING agonists, including cGAMP, CDA (Invivogen), 2′3′-cGAM(PS)2 (Rp/Sp) (Invivogen), ADU-S100 (MedChemExpress) and diABZI (MedChemExpress), were added to 1×10^5 THP1 reporter cells in 96-well plates. After incubation for 24 h at 37 °C under 5% CO_2, the supernatants were collected and assessed for IFNβ by ELISA.

Synthesis and characterization of CDN–Mn/Zn coordination polymers, CMP_{CDA}, CZP_{CDA} and CDA liposomes. CDA, CDG or cGAMP (Invivogen) was dissolved in methanol to give 1 mg ml^{-1} solutions. $MnCl_2$ or $ZnCl_2$ (Sigma-Aldrich) was dissolved in methanol to prepare 100 mM stock solutions. In a typical synthesis reaction, $MnCl_2$ or $ZnCl_2$ solution was added to 1 mg ml^{-1} CDN solution in a 10:1 (n/n) ratio under vigorous stirring. The mixture was sonicated for 1 min and then stirred for another 1 h at room temperature. The resulting CDN–Mn was centrifuged at 20,000*g* for 10 min to remove free CDNs and metal ions, followed by washing with methanol.

The CMPs were synthesized according to a method adapted from previous reports[58–60]. First, DOPE-H11 was synthesized by the reaction of dioleoyl-sn-glycero-3-phosphoethanolamine-N-(succinimidyloxy-glutaryl) (DOPE-NHS) and H11 (2 equiv.) in *N*,*N*-dimethylformamide, purified by dialysis using 2 kilodaltons (kD) molecular weight cut-off (MWCO) dialysis tubes, and characterized by HPLC. A mixture containing 1 ml of 1 mg ml^{-1} CDA in methanol, 0.14 ml of 100 mM $MnCl_2$ in methanol and 2 ml of 2 mg ml^{-1} DOPE-H11 in ethanol was sonicated and then vortexed overnight, followed by centrifugation at 20,000*g* for 10 min. The resulting CDA–Mn@DOPE was resuspended in ethanol containing DOPC–cholesterol–DSPE-PEG5000 (4:1:1), sonicated and added to a solution of 30% (v/v) ethanol–H_2O. Lastly, the CMPs were obtained by evaporating the organic solvent under reduced pressure and washing with 10% sucrose using 100 kD (MWCO) centrifugal ultrafiltration. The CZPs were synthesized using the same method except for replacing $MnCl_2$ with $ZnCl_2$. CDA liposomes were synthesized as reported previously[18].

The loading of CDA in the CMPs, CZPs and CDA liposomes was quantified by UV absorbance at 260 nm, followed by verification by HPLC. The loading of Mn^{2+} in the CMPs was quantified by inductively coupled plasma-mass spectrometry (ICP-MS; Perkin-Elmer Nexion 2000) and verified by thermogravimetric analysis (Discovery TGA, TA Instruments). The size and surface charge of the CMPs were measured using a Zetasizer (Nano ZSP). The morphology of CDN–Mn was observed by TEM. All images were acquired on a JEM 1200EX electron microscope (JEOL) equipped with an AMT XR-60 digital camera (Advanced Microscopy Techniques).

In vitro evaluation of BMDC activation, cellular uptake and STING activation. The BMDCs were prepared as described previously[57]. Briefly, bone marrow was collected and plated in bacteriological Petri dishes with culture media containing granulocyte–macrophage colony-stimulating factor. The cell culture media were refreshed on days 3, 6 and 8. After 8 days of differentiation, the BMDCs were collected for use. To observe BMDC activation by CDNs and Mn^{2+}, BMDCs, seeded in 12-well plates at 1×10^6 cells per well, were incubated with 5 μM CDA and/or 250 μM Mn^{2+} for 24 h. The treated BMDCs were collected, washed with fluorescence-activated cell sorting (FACS) buffer (1% BSA in PBS), incubated with anti-CD16/32 at room temperature and then stained on ice with fluorophore-labelled antibodies against CD11c, CD80 and CD86. The cells were then washed twice with FACS buffer, resuspended in 2 μg ml^{-1} 4′,6-diamidino-2-phenylindole (DAPI) solution and analysed by flow cytometry (Ze 5 with Everest Software (v.3.0.75), Bio-Rad). The data were processed using FlowJo (v.10.5).

To visualize and quantify the cellular uptake of STING agonist, a fluorophore-labelled CDN, CDG-Dy547 (Biolag), was admixed with CDA (1:10, n/n) to prepare CDG-Dy547@CMP_{CDA} following the same synthesis procedure as used for CMP_{CDA} mentioned above. The loading of CDG-Dy547 in the CMPs was quantified by absorbance at 550 nm. Next, 1×10^6 BMDCs were seeded on 35 mm Petri dishes (MatTek) and incubated with CDG-Dy547 in free form or in CDG-Dy547@CMP_{CDA} for 6, 12 or 24 h. For confocal imaging, the cells were washed three times with PBS, incubated with 50 nM LysoTracker green DND-99 (Invitrogen) for 30 min at 37 °C to stain the lysosomes and then imaged using a confocal microscope (Nikon A1). For cellular uptake quantification, the cells were collected and washed with FACS buffer (1% BSA in PBS). The fluorescence of CDG-Dy547 was analysed by flow cytometry (Ze 5 with Everest Software (v.3.0.75), Bio-Rad) and the data were processed using FlowJo (v.10.5).

To measure the STING activation of CDA and/or Mn^{2+} in free form or in CMP_{CDA}, BMDCs were seeded at 1×10^5 cells per well in 96-well plates and incubated with CDA and/or Mn^{2+} in free form or in CMP_{CDA} (containing 2.5 μM CDA or/and 15.6 μM Mn^{2+}). After incubation for 24 h at 37 °C under 5% CO_2, the supernatants were collected for ELISA assay of cytokines in the Cancer Center Immunology Core of the University of Michigan.

In vivo cancer immunotherapy. All animals were cared for following federal, state and local guidelines. All work performed on animals was in accordance with and approved by the Institutional Animal Care and Use Committee (IACUC) at the University of Michigan. For the CT26 murine tumour model, female BALB/c mice of age 6–8 weeks (Jackson Laboratories) were inoculated with 1.5×10^5 CT26 colon cancer cells subcutaneously in the right back flank. For the CT26 two-tumour model, 3×10^5 and 1×10^5 CT26 tumour cells were inoculated in the right (primary) and left (distal) flank, respectively. For the B16F10 tumour model, C57BL/6 mice (Jackson Laboratory) were inoculated with the indicated number of B16F10 cells subcutaneously in the right flank. Tumour-bearing mice were randomly assigned to different treatment groups. The indicated drugs or formulations were administered by the indicated route at the indicated time points. Tumour size and survival were monitored every 2–4 days. Tumour size was calculated based on the equation: volume = length × width^2 × 0.5. Animals were euthanized when the tumour reached 1.5 cm in diameter or when they became moribund with severe weight loss or unhealing ulceration. At the indicated time points, the cytokine levels in serum were measured by ELISA assay in the Cancer Center Immunology Core of the University of Michigan. The percentages of tumour antigen-specific CD8α+ T cells among PBMCs were analysed using the tetramer staining assay, as described previously for AH1 peptide–major histocompatibility complex (MHC) tetramer (H-2L^d-restricted AH1 (SPSYVYHQF); NIH Tetramer Core Facility, Atlanta). ELISPOT assays were performed with PBMCs from the treated mice, as described previously[61].

NOOC1 (Kerafast, EMU061) was maintained in IMDM medium (Gibco, 12440053). To prepare 1 l of growth medium for NOOC1, 626 ml IMDM base was mixed with 313 ml F-12 nutrient mix (Gibco, 11765054), 50 ml fetal bovine serum (FBS) (Hyclone, SH3039603), 10 ml Pen Strep (Thermo Fisher, 15-140-122), 1.25 ml of 4 mg ml^{-1} insulin (Invitrogen, 12585014), 200 μl of 200 μg ml^{-1} hydrocortisone (Sigma-Aldrich, H0888-1G) and 50 μl of 100 μg ml^{-1} epidermal growth factor (EMD Millipore, 01-107). For in vivo implantation, Matrigel (Thermo Fisher, CB-40230) was thawed overnight at 4 °C. On the day of injection, NOOC1 was washed once with PBS and mixed with Matrigel to reach a density of 2×10^7 cells ml^{-1}. Each mouse was inoculated subcutaneously with 2×10^6 cells (100 μl). Tumour size and survival were monitored every 2 or 3 days as indicated above.

In vivo immune response analysis. Phenotypic and functional assessments of T cells in PBMCs were conducted. Briefly, the PBMCs were collected after removing red blood cells using ACK lysis buffer. The PBMCs were blocked with CD16/32 antibody for 10 min. To analyse tumour antigen-specific CD8$^+$ T cell response and memory phenotype, cell pellets were first stained with phycoerythrin (PE)-tagged AH1 peptide–MHC tetramer and then further stained with allophycocyanin (APC) rat anti-mouse CD8a (clone: 53-6.7 (RUO), BD Biosciences), fluorescein isothiocyanate (FITC) rat anti-human/mouse CD44 (clone: IM7, eBioscience) and PE-Cy7 CD62L monoclonal antibody (clone: MEL-14, eBioscience). Stained cells were incubated with DAPI prior to flow cytometry analysis (Ze5 with Everest Software (v.3.0.75), Bio-Rad).

For the IFNγ ELISPOT assay, the ELISPOT plate was coated with IFNγ capture antibody for 24 h and blocked with Dulbecco's modified Eagle medium containing 10% FBS for 2 h. The PBMCs obtained from treated mice were added to 96-well plates with a fixed number of live cells per well. The SPSYVYHQF peptide (20 μg ml^{-1}) was added to stimulate the PBMCs. Ionomycin and phorbol myristate acetate were employed as positive control. After 18 h, IFNγ spots were detected with biotinylated detection antibody, followed by streptavidin–horseradish peroxidase and 3-amino-9-ethylcarbazole substrate kit. The IFNγ spot number and size were measured in the Cancer Center Immunology Core at the University of Michigan.

Tumour tissues were analysed as described before[52]. Tumour tissues were excised at preset time points, cut into small pieces and treated additionally with collagenase type IV (1 mg ml^{-1}) and DNase I (0.1 mg ml^{-1}) under gentle shaking. After 30 min, the cell suspension was filtered through a 70-μm strainer. The cells were washed with FACS buffer and blocked with CD16/32 antibody. Cells were then stained with the following designated antibody panels: APC/Cy7 anti-mouse CD45 antibody (clone: 30-F11, BioLegend), Pacific blue anti-mouse CD8a antibody (clone: 53-6.7, BioLegend), FITC rat anti-mouse CD49b (clone: DX5, BioLegend), BV786 anti-CD3 antibody (clone: 17A2, BD Biosciences), APC anti-mouse CD107a antibody (1D4B (RUO), BD Biosciences), PE-Cy7 anti-mouse CD11c antibody (clone: HL3 (RUO), BD Biosciences), FITC anti-MHC-II antibody (clone: M5/114.15.2, eBioscience) and BV605 anti-mouse CD86 antibody (clone: GL1, BD Biosciences); Pacific blue anti-mouse CD45 antibody (clone: 30-F11, BioLegend), APC-Cy7 anti-mouse CD3 antibody (clone: 17A2, BD Biosciences),

APC anti-mouse CD8a antibody (clone: 53-6.7 (RUO), BD Biosciences), FITC rat anti-mouse CD49b (clone: DX5, BioLegend), BV786 anti-CD3 antibody (clone: 17A2, BD Biosciences), PE-Cy7 anti-mouse CD11c antibody (clone: HL3 (RUO), BD Biosciences), FITC anti-MHC-II antibody (clone: M5/114.15.2, eBioscience), BV605 anti-mouse/human CD11b (clone: M1/70, BioLegend), PE anti-mouse F4/80 (clone: BM8, BioLegend), APC anti-mouse CD206 (MMR, clone: C068C2, BioLegend), PE-Cy7 anti-mouse CD86 antibody (clone: GL1, BD Biosciences) and FITC anti-mouse Ly-6C antibody (clone: AL-21, BD Biosciences); BV421 anti-mouse Ly-6G antibody (clone: RB6-8C5, BioLegend); BV605 anti-mouse CD45 antibody (clone: 30-F11, BioLegend), APC/Cy7 anti-mouse/human CD11b antibody (clone: M1/70, BioLegend), PE anti-mouse F4/80 antibody (clone: BM8, BioLegend), APC anti-mouse CD206 antibody (MMR, clone: C068C2, BioLegend), PE-Cy7 anti-mouse CD86 antibody (clone: GL1, BD Biosciences), BV421 anti-mouse Ly-6G antibody (clone: RB6-8C5, BioLegend) and FITC anti-mouse Ly-6C antibody (clone: AL-21, BD Biosciences). The stained cells were analysed by cytometry (MoFlo Astrios Cell Sorter, Beckman). The data were processed using FlowJo (v.10.5).

In vivo drug distribution analysis. To analyse the in vivo biodistribution of STING agonist, CDG-Dy547 (Biolag) or CDG-Cy7 (Biolag) was admixed with CDA (1:10, n/n) to prepare CDG-Dy547@CMP_{CDA} or CDG-Cy7@CMP_{CDA} following the same synthesis procedure as used for CMP_{CDA} described above. The loading of CDG-Dy547 and CDG-Cy7 were quantified by absorbance at 550 or 750 nm, respectively. To quantify drug retention at the tumour site after intratumoural injection, CDG-Cy7 in free form or in CMP_{CDA} was injected into the tumours. Mice were imaged by IVIS optical imaging at different time points (0, 4, 8 or 24 h), and the fluorescence signal of CDG-Cy7 in the tumours was measured accordingly. Drug retention was calculated by normalizing the remaining fluorescence signal of CDG-Cy7 in the tumour at the indicated time point by that of the injected CDG-Cy7 at 0 h. To quantify the biodistribution of CMPs after i.v. administration, CDG-Cy7 in free form or in CMP_{CDA} was injected intravenously. Mice were euthanized 24 h post-injection, and the fluorescence intensity in the major organs was measured accordingly. To quantify the biodistribution of Mn, tissues were digested by microwave, and the amount of Mn was measured using ICP-MS by the Michigan Elemental Analysis Laboratory.

To analyse drug distribution in the TME, CDG-Dy547@CMP_{CDA} was injected by the i.t. or i.v. route. At the indicated time point, cells were collected from the TME and stained, as mentioned above. The amount of phagocytosed CDG-Dy547 in different cell populations was analysed by FACS. The cells were then stained with the following designated antibodies panels: Pacific blue anti-mouse CD45 antibody (clone: 30-F11, BioLegend), BV605 anti-mouse CD3 antibody (clone: 17A2, BioLegend), APC anti-mouse CD11c antibody (clone: N418, BioLegend), FITC anti-MHC-II antibody (clone: M5/114.15.2, eBioscience), BV605 anti-mouse/human CD11b antibody (clone: M1/70, BioLegend), APC anti-mouse F4/80 antibody (clone: BM8, BioLegend) and FITC anti-mouse Ly-6C antibody (clone: AL-21, BD Biosciences). The stained cells were analysed by cytometry (MoFlo Astrios Cell Sorter, Beckman). The data were processed using FlowJo (v.10.5).

Statistical analysis. The results are expressed as means ± standard error of the mean (s.e.m.). One- or two-way ANOVA analysis, followed by Bonferroni's multiple comparisons post hoc test or two-tailed multiple *t*-tests with Bonferroni–Dunn correction, was used for testing differences among groups. The data were approximately normally distributed, and variance was similar between groups. Experiments were repeated multiple times as independent experiments, as indicated in the figure captions. Shown in each figure is a complete dataset from one representative, independent experiment. No samples were excluded from analysis. GraphPad Prism 8.0 (GraphPad Software) was used for statistical analyses.

Reporting Summary. Further information on research design is available in the Nature Research Reporting Summary linked to this article.

Data availability

The authors declare that data supporting the findings of this study are available within the article and its Supplementary Information files. All relevant data can be provided by the authors upon reasonable request.

Acknowledgements

This work was supported in part by the NIH (R01AI127070, R01CA210273, U01CA210152, R01DK108901, R01DE026728 and R01DE030691), a University of Michigan Rogel Cancer Center Support Grant (P30CA46592) and the University of Michigan, Michigan Drug Discovery (MDD21102). J.J.M. is supported by an NSF CAREER Award (1553831). L.W. was supported in part by the NIH (U24CA232979 and R01CA255242). X. Sun is supported by a Rackham International Student Fellowship and a Rackham Predoctoral Fellowship. We acknowledge J. Hong at the University of Michigan for helping with the ITC analysis, A. Dial at the Michigan Element Analysis Laboratory for Mn biodistribution analysis, K. Chinnaswamy at the University of Michigan Center for Structural Biology for helping with the protein thermal shift assay, J. Whitfield at the University of Michigan Cancer Center Immunology Core for ELISA analysis, H. Carlson at the University of Michigan for molecular dynamic analysis and Q. Zheng at Fujian Medical University Union Hospital for histological analysis. We also thank the University of Michigan Flow Cytometry Core, the ULAM (Unit for Laboratory Animal Medicine) In Vivo Animal Core (IVAC), and the University of Michigan Microscope Imaging Core for technical assistance. We acknowledge the NIH Tetramer Core Facility (contract HHSN272201300006C) for the provision of MHC-I tetramers.

Author contributions

X. Sun, Y.L.L. and J.J.M. designed the experiments. X. Sun performed the experiments. Y.Z., J.L., K.S.P., K.H., X.Z., Y.X., J.N., J.X., X. Shi and L.W. helped with specific experiments. J.L. contributed to the western blotting assays. L.W. and Y.L.L. produced the NOOC1 model and characterized its mutational landscape and response profiles to immunotherapies. Y.X. contributed to the ELISPOT assay. X. Sun, J.L., L.W., Y.L.L. and J.J.M. analysed and interpreted the data. X. Sun, Y.L.L. and J.J.M. wrote the paper.

Competing interests

A patent application (WO2020014644A1) for CMP-based metalloimmunotherapy has been filed, with J.J.M. and X. Sun as inventors. Y.L.L. has licensed the NOOC1 model to Kerafast Inc. (catalogue number: EMU061). The remaining authors declare no competing interests.

Additional information

Supplementary information The online version contains supplementary material available at https://doi.org/10.1038/s41565-021-00962-9.

Correspondence and requests for materials should be addressed to James J. Moon.

Peer review information *Nature Nanotechnology* thanks Jeffrey Hubbell and the other, anonymous, reviewer(s) for their contribution to the peer review of this work.

nature research

Corresponding author(s): James J. Moon

Last updated by author(s): Jul 12, 2021

Reporting Summary

Nature Research wishes to improve the reproducibility of the work that we publish. This form provides structure for consistency and transparency in reporting. For further information on Nature Research policies, see our Editorial Policies and the Editorial Policy Checklist.

Statistics

For all statistical analyses, confirm that the following items are present in the figure legend, table legend, main text, or Methods section.

n/a	Confirmed
☐	☒ The exact sample size (*n*) for each experimental group/condition, given as a discrete number and unit of measurement
☐	☒ A statement on whether measurements were taken from distinct samples or whether the same sample was measured repeatedly
☐	☒ The statistical test(s) used AND whether they are one- or two-sided *Only common tests should be described solely by name; describe more complex techniques in the Methods section.*
☐	☒ A description of all covariates tested
☐	☒ A description of any assumptions or corrections, such as tests of normality and adjustment for multiple comparisons
☐	☒ A full description of the statistical parameters including central tendency (e.g. means) or other basic estimates (e.g. regression coefficient) AND variation (e.g. standard deviation) or associated estimates of uncertainty (e.g. confidence intervals)
☐	☒ For null hypothesis testing, the test statistic (e.g. *F*, *t*, *r*) with confidence intervals, effect sizes, degrees of freedom and *P* value noted *Give P values as exact values whenever suitable.*
☒	☐ For Bayesian analysis, information on the choice of priors and Markov chain Monte Carlo settings
☐	☒ For hierarchical and complex designs, identification of the appropriate level for tests and full reporting of outcomes
☐	☒ Estimates of effect sizes (e.g. Cohen's *d*, Pearson's *r*), indicating how they were calculated

Our web collection on statistics for biologists contains articles on many of the points above.

Software and code

Policy information about availability of computer code

Data collection	Flow cytometric data were collected using ZE5 Everest Software v.3.0.75. In vivo images were acquired using IVIS Lumina Living Image Software(v.4.5.5). DLS analysis was colleted in Zetasizer software version 7.13. Thermal shift assay were aquired using LightCycler® Software 4.1.
Data analysis	Flow cytometry analysis was done in Everest Software v.3.0.75 and FlowJo (v.10.5) (Tree Star). In vivo images were analyzed using IVIS Lumina Living Image (v.4.5.5) Software. Statistical analysis was done in GraphPad Prism 8.0. DLS analysis was done in Zetasizer software version 7.13.Thermal shift assay were analyzed using LightCycler® Software 4.1. Western blotting data were analyzed by ImageJ bundled with Java 1.8.0_172.

For manuscripts utilizing custom algorithms or software that are central to the research but not yet described in published literature, software must be made available to editors and reviewers. We strongly encourage code deposition in a community repository (e.g. GitHub). See the Nature Research guidelines for submitting code & software for further information.

Data

Policy information about availability of data

All manuscripts must include a data availability statement. This statement should provide the following information, where applicable:

- Accession codes, unique identifiers, or web links for publicly available datasets
- A list of figures that have associated raw data
- A description of any restrictions on data availability

The authors declare that data supporting the findings of this study are available within the article and its Supplementary Information files. All relevant data can be provided by the authors upon reasonable request. The raw and analysed datasets generated during the study are too large to be publicly shared, yet they are available for research purposes from the corresponding author on reasonable request.

Field-specific reporting

Please select the one below that is the best fit for your research. If you are not sure, read the appropriate sections before making your selection.

☒ Life sciences ☐ Behavioural & social sciences ☐ Ecological, evolutionary & environmental sciences

For a reference copy of the document with all sections, see nature.com/documents/nr-reporting-summary-flat.pdf

Life sciences study design

All studies must disclose on these points even when the disclosure is negative.

Sample size	Sample sizes were chosen based on our preliminary data from at least two pilot experiments and previously published results in the literature (doi.org/10.1038/s41565-018-0342-5, doi.org/10.1038/nmat4822).
Data exclusions	No data were excluded.
Replication	All experiments were repeated at least twice with similar results
Randomization	Mice were assigned randomly to experimental groups.
Blinding	The investigators were not blinded to allocation during experiments and outcome assessment since our data analyses are based on objectively measurable data.

Reporting for specific materials, systems and methods

We require information from authors about some types of materials, experimental systems and methods used in many studies. Here, indicate whether each material, system or method listed is relevant to your study. If you are not sure if a list item applies to your research, read the appropriate section before selecting a response.

Materials & experimental systems

n/a	Involved in the study
☐	☒ Antibodies
☐	☒ Eukaryotic cell lines
☒	☐ Palaeontology and archaeology
☐	☒ Animals and other organisms
☒	☐ Human research participants
☒	☐ Clinical data
☒	☐ Dual use research of concern

Methods

n/a	Involved in the study
☒	☐ ChIP-seq
☐	☒ Flow cytometry
☒	☐ MRI-based neuroimaging

Antibodies

Antibodies used	APC-CD8a rat anti-mouse (Clone: 53-6.7(RUO), BD Biosciences), FITC-CD44 rat anti-human/mouse (Clone: IM7, eBioscience) , PE-Cy7-CD62L monoclonal antibody (Clone: MEL-14, eBioscience), APC-Cy7-Anti-mouse CD45 Antibody (Clone: 30-F11, BioLegend), Pacific Blue-Anti-mouse CD8a Antibody (Clone: 53-6.7, BioLegend), FITC Rat Anti-mouse CD49b (Clone: DX5, BioLegend), BV786-Anti-CD3 Antibody (Clone: 17A2, BD Biosciences), APC-Anti-mouse CD107a Antibody (1D4B (RUO), BD Biosciences), PE-Cy7- Anti-mouse CD11c Antibody (Clone: HL3 (RUO), BD Biosciences), FITC-Anti-MHC-II Antibody (Clone: M5/114.15.2, eBioscience), BV605-Anti-mouse CD86 Antibody (Clone: GL1, BD Bioscience); Pacific Blue-Anti-mouse CD45 Antibody (Clone: 30-F11, BioLegend), APC-Cy7-Anti-mouse CD3 Antibody (Clone: 17A2, BD Bioscience), APC-Anti-mouse CD8a Antibody (Clone: 53-6.7(RUO), BD Biosciences), FITC Rat Anti-mouse CD49b (Clone: DX5, BioLegend), BV786-Anti-CD3 Antibody (Clone: 17A2, BD Biosciences), PE-Cy7- Anti-mouse CD11c Antibody (Clone: HL3 (RUO), FITC-Anti-MHC-II Antibody (Clone: M5/114.15.2, eBioscience), BV605-Anti-mouse/human CD11b (Clone: M1/70, BioLegend), PE-Anti-mouse F4/80 (Clone: BM8, BioLegend), APC-Anti-mouse CD206 (MMR, Clone: C068C2, BioLegend), PE-Cy7-Anti-mouse CD86 Antibody (Clone: GL1, BD Bioscience), FITC-Anti-mouse Ly6C Antibody (Clone: AL-21, BD Bioscience); BV421-Anti-mouse Ly6G Antibody (Clone: RB6-8C5, BioLegend); BV605-Anti-mouse CD45 Antibody (Clone: 30-F11, BioLegend), APC-Cy7-Anti-mouse/human CD11b (Clone: M1/70, BioLegend), PE-Anti-mouse F4/80 (Clone: BM8, BioLegend), APC-Anti-mouse CD206 (MMR, Clone: C068C2, BioLegend), PE-Cy7-Anti-mouse CD86 Antibody (Clone: GL1, BD Bioscience), BV421-Anti-mouse Ly6G Antibody (Clone: RB6-8C5, BioLegend), FITC-Anti-mouse Ly6C Antibody (Clone: AL-21, BD Bioscience), Pacific Blue-anti-mouse CD45 antibody (Clone: 30-F11, BioLegend), BV605-anti-mouse CD3 antibody (Clone: 17A2, BioLegend), APC-anti-mouse CD11c antibody (Clone: N418, BioLegend), FITC-anti-MHC-II antibody (Clone: M5/114.15.2, eBioscience), BV605-anti-mouse/human CD11b (Clone: M1/70, BioLegend), APC-anti-mouse F4/80 (Clone: BM8, BioLegend), FITC-anti-mouse Ly6C antibody (Clone: AL-21, BD Bioscience).
Validation	Antibody validation was provided by manufacture's website (cell images) and/or data provided in the manuscript.

Eukaryotic cell lines

Policy information about cell lines

Cell line source(s)	THP1-hSTING HAQ, CT26 and B16F10 cell lines were obtained from the American Type Culture Collection (ATCC). THP1 hSTING H232 and THP1 hSTING R232 cell lines were purchased from Invivogen. NOOC1 cell line was developed in house.
Authentication	THP1-hSTING HAQ, CT26 and B16F10 cell lines were authenticated by ATCC. THP1 hSTING H232 and THP1 hSTING R232 cell lines were authenticated by Invivogen.
Mycoplasma contamination	All cell lines were tested negative for mycoplasma contamination.
Commonly misidentified lines (See ICLAC register)	No commonly misidentified cell lines were used.

Animals and other organisms

Policy information about studies involving animals; ARRIVE guidelines recommended for reporting animal research

Laboratory animals	For in vivo studies, 6-8-week-old female BALB/c mice (Jackson Laboratory, or Taconic Farm, or Charles River, 18 g-20 g) and 6-8-week-old female C57-BL/6 mice (Jackson Laboratory, 18 g-20 g) were used and housed in 12 light/12 dark cycle, 65-75°F (~18-23°C), 40-60% humidity condition.
Wild animals	No wild animals were used.
Field-collected samples	No field-collected samples were used.
Ethics oversight	All work performed on animals was in accordance with and approved by the Institutional Animal Care & Use Committee (IACUC) at University of Michigan, Ann Arbor.

Note that full information on the approval of the study protocol must also be provided in the manuscript.

Flow Cytometry

Plots

Confirm that:

☒ The axis labels state the marker and fluorochrome used (e.g. CD4-FITC).

☐ The axis scales are clearly visible. Include numbers along axes only for bottom left plot of group (a 'group' is an analysis of identical markers).

☒ All plots are contour plots with outliers or pseudocolor plots.

☒ A numerical value for number of cells or percentage (with statistics) is provided.

Methodology

Sample preparation	The sample preparation was described in the Methods.
Instrument	Bio-Rad Ze5
Software	Everest Software v.3.0.75 was used for collection. Everest Software and FlowJo were used for analysis.
Cell population abundance	Data on the abundance of relevant cell populations are provided in the manuscript.
Gating strategy	Cells were gated first by morphology to exclude cell debris, doublets were then gated out by FSC-A/FSC-W, followed by exclusion of dead cells by gating on dye negative cells.

☒ Tick this box to confirm that a figure exemplifying the gating strategy is provided in the Supplementary Information.

nature portfolio

https://doi.org/10.1038/s41565-021-00962-9

Supplementary information

Amplifying STING activation by cyclic dinucleotide–manganese particles for local and systemic cancer metalloimmunotherapy

In the format provided by the authors and unedited

Supplementary Information for

Amplifying STING Activation by Cyclic Dinucleotide-Manganese Particles for Local and Systemic Cancer Metalloimmunotherapy

Xiaoqi Sun[1, 3], Yu Zhang[1], Jiaqian Li[5], Kyung Soo Park[2, 3], Kai Han[1, 3], Xingwu Zhou[1, 3], Yao Xu[1, 3], Jutaek Nam[1, 3, 4], Jin Xu[1, 3], Xiaoyue Shi[1, 3], Lei Wei[5], Yu Leo Lei[6, 7, 8], James J. Moon[1, 2, 3, 8]

[1]Department of Pharmaceutical Sciences, University of Michigan, Ann Arbor, Michigan 48109, USA.

[2]Department of Biomedical Engineering, University of Michigan, Ann Arbor 48109 USA.

[3]Biointerfaces Institute, University of Michigan, Ann Arbor, Michigan 48109, USA.

[4]College of Pharmacy, Chonnam National University, Gwangju 61186, Republic of Korea.

[5]Department of Biostatistics and Bioinformatics, Roswell Park Comprehensive Cancer Center, Buffalo, NY, 14203, USA.

[6]Department of Periodontics and Oral Medicine, University of Michigan, Ann Arbor, MI 48109, USA.

[7]Department of Otolaryngology – Head and Neck Surgery, University of Michigan, Ann Arbor, MI 48105, USA

[8]Rogel Cancer Center, University of Michigan, Ann Arbor, MI 48109, USA.

*E-mail: moonjj@umich.edu

Supplementary Materials and Methods

In vitro protein thermal shift assay

The thermal shift assay of STING-STING agonist complexes was conducted as described previously[1]. STING agonists (cGAMP, CDA, ADU-S100, di-ABZI) and human recombinant STING proteins, including $hSTING^{R232}$ and $hSTING^{H232}$ (Cayman Chemical), were dissolved in TSA buffer (150 mM NaCl, 50 mM HEPES pH 7.4). STING agonists and STING proteins were mixed in three buffer conditions: 1) with 10 mM $MnCl_2$, 2) without $MnCl_2$ (HEPES), or 3) with 10 mM $MnCl_2$ + 100 mM EDTA. The final concentrations of the ligand and protein were 150 μM and 4 μM, respectively. The mixtures were incubated on ice for 10 min. SYPRO Orange Protein Gel Stain (Sigma–Aldrich) was subsequently added (final 5x concentration), and the mixtures were again incubated on ice for a further 10 min. Protein melting curves were measured with Roche LightCycler QPCR instrument and analyzed by LightCycler software.

Production of the NOOC1 tobacco-associated squamous cell carcinoma model syngeneic to C57BL/6J

To generate NOOC1 tumor model, 4NQO (N8141, Millipore Sigma) was dissolved in propylene glycol to produce the 4 mg/ml stock solution. A final concentration of 50 μg/ml was reached by diluting the stock solution in drinking water. C57BL/6J mice (5 weeks of age) were fed with 4-NQO-containing drinking water for 16 weeks. Water bottles were changed weekly. After the 16-week challenge period, mice were fed with regular drinking water and monitored twice per week to assess oral lesions. Visible oral squamous cell carcinoma tissue was homogenized to produce single-cell suspensions. Then, viable EpCAM+ tumor cells were sorted by flow cytometry to generate single-cell clones. After repetitive passages, single-cell clones that were able to produce stable cell lines *in vitro* were screened *in vivo* for their tumorigenic potential. A single-cell clone (NOOC1) was confirmed to stably produce tumors when implanted in syngeneic C57BL/6J hosts. Whole exome sequencing was performed to characterize the mutational landscape. The sequencing data were deposited in the NCBI Sequence Read Archive with the BioProject ID: PRJNA701422.

The bioinformatics analysis utilized high-quality paired-end reads passing Illumina RTA filter -aligned to the NCBI human reference genome (GRCh37) using BWA. PCR duplicated reads are marked and removed by using Picard (http://picard.sourceforge.net/). Putative single-nucleotide variants (SNVs) and small insertions/deletions (Indels) were identified by running two different variant callers Strelka[2] and Mutect[3]. Potential

false positives introduced by sequencing and mapping artifacts were filtered out as previously described[4-6]. The identified somatic mutations were compared to the public human germline databases including dbSNP[7], 1000 Genomes Project[8], National Heart, Lung, and Blood Institute's Exome Sequencing Project, and The Genome Aggregation Database (gnomAD) to remove germline polymorphisms. All mutations were annotated by ANNOVAR[6] using NCBI RefSeq database. The mutational signatures of SNVs in NOOC1 and 4MOSC cell lines were analyzed using SigProfilerSingleSample[5].

Supplementary Figures

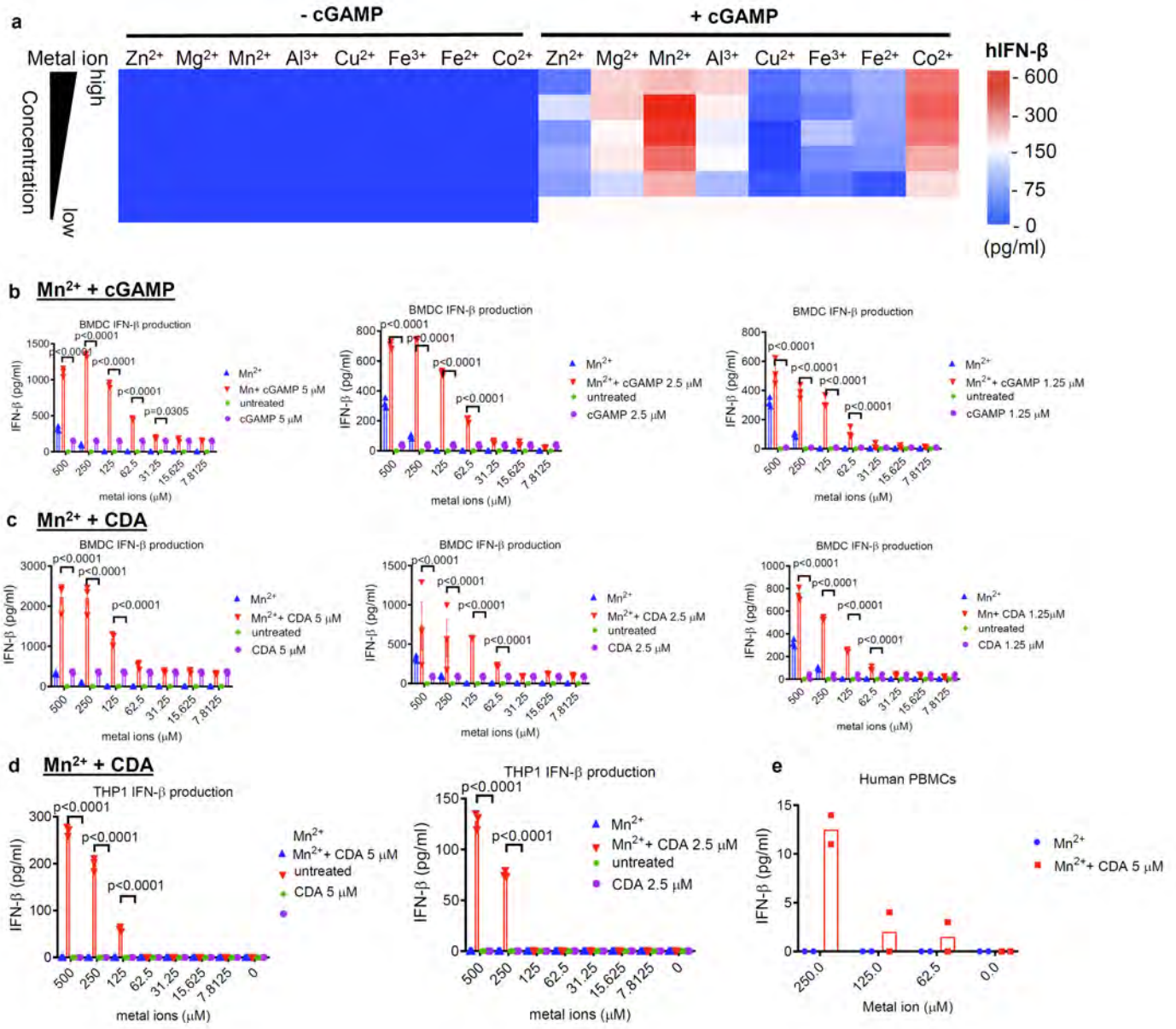

Supplementary Figure 1. Mn^{2+} augments type-I IFN activity of STING agonists. a) Screening of metal ions for augmenting type-I IFN response of STING agonists in THP1 cells. THP1 monocyte cells were incubated with various concentrations of metal ions (0-500 μM) ± cGAMP, and after 24 h, human IFN-β secretion was quantified by ELISA. **b-c)** BMDCs were treated with various concentrations of Mn^{2+} with either cGAMP (b) or c-di-AMP (CDA) (c), after 24 h, mouse IFN-β secretion was quantified by ELISA. **d-e**) Human THP1 cells (d) or primary human PBMCs (e) were treated with various concentrations of Mn^{2+} ± CDA, and after 24 h, hIFN-β secretion was quantified by ELISA. Data represent mean ± SEM, from a representative experiment from 2 independent experiments with *n* = 3 (b-d) or n = 2 (e) biologically independent replicates. Data were analyzed by two-way ANOVA with Bonferroni's multiple comparisons test (b-d).

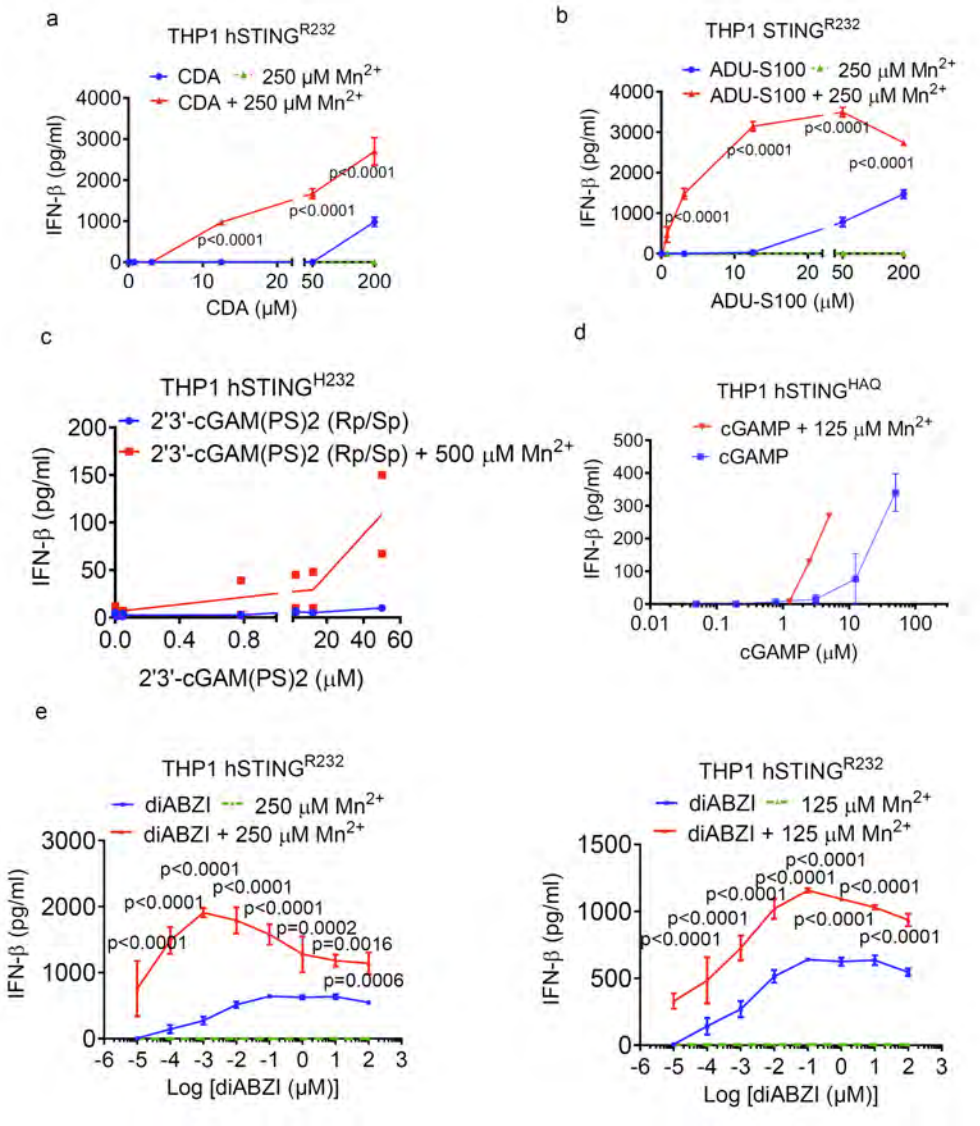

Supplementary Figure 2. Mn^{2+} augments type-I IFN activity of CDN- and non-CDN-based STING agonists. **a-b)** THP1 cells expressing hSTING^{R232} were incubated with Mn^{2+} and various concentrations of CDA (a) or ADU-S100 (b). After 24 h, hIFN-β secretion was quantified by ELISA. **c)** THP1 cells expressing hSTING^{H232} were incubated with Mn^{2+} and various concentrations of 2'3'-cGAM(PS)2 (Rp/Sp), and after 24 h, hIFN-β secretion was quantified by ELISA. **d)** THP1 cells expressing hSTING^{HAQ} were incubated with Mn^{2+} and various concentrations of cGAMP, and after 24 h, hIFN-β secretion was quantified by ELISA. **e)** THP1 cells expressing hSTING^{R232} were incubated with Mn^{2+} and various concentrations of diABZI, and after 24 h, hIFN-β secretion was quantified by ELISA. Data represent mean ± SEM, from a representative experiment from 2 independent experiments with *n* = 3-4 (a-b, d-e) or n = 2 (c) biologically independent replicates. Data were analyzed by two-way ANOVA with Bonferroni's multiple comparisons test (a-b, d-e).

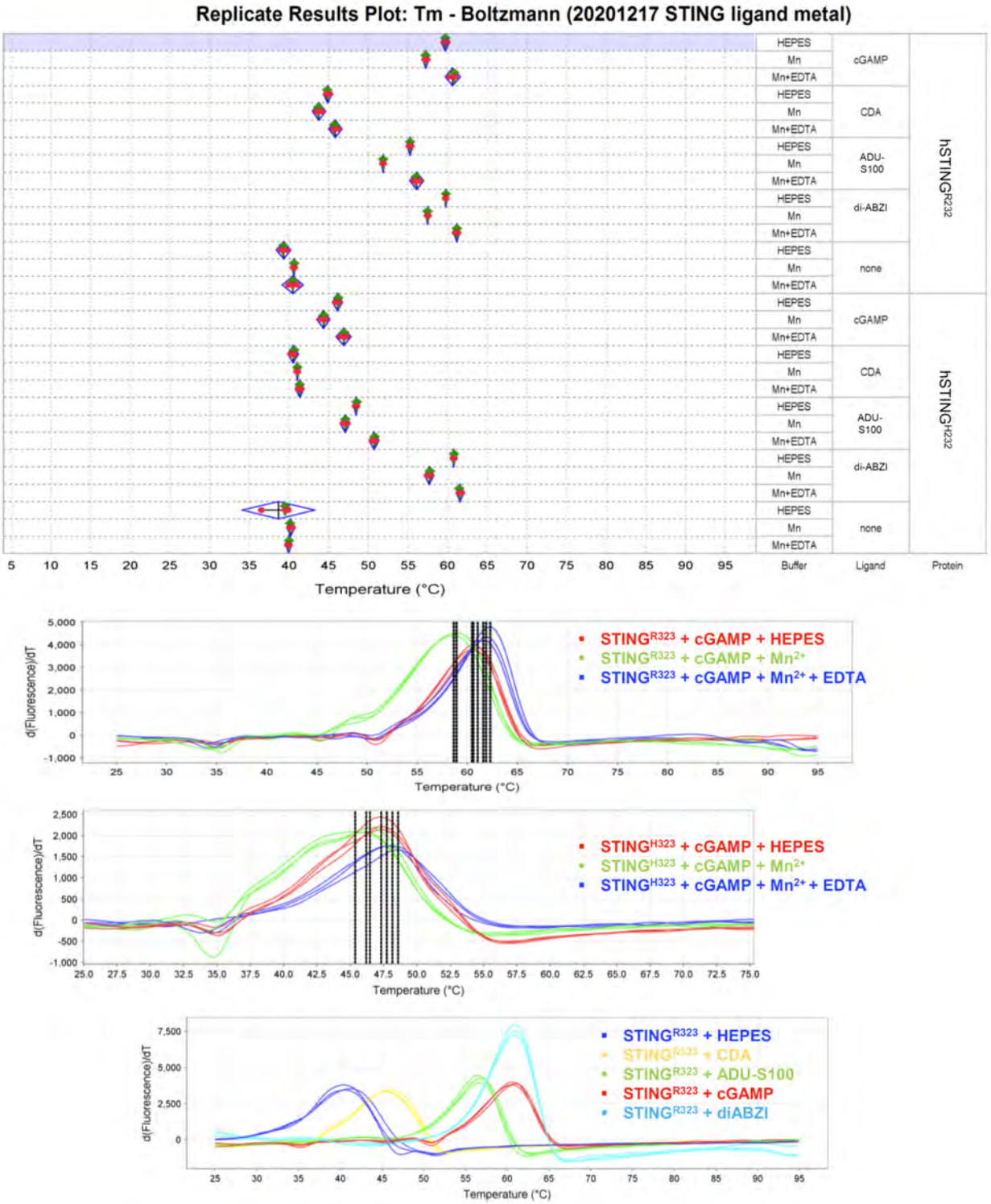

Supplementary Figure 3. Thermal shift assay of STING-STING agonist complexes with Mn^{2+} or without Mn^{2+}. The thermal shift assay of STING-STING agonist complexes was conducted according as reported previously[1]. STING agonists (cGAMP, CDA, ADU-S100, di-ABZI) and human recombinant STING proteins, $hSTING^{R232}$ and $hSTING^{H232}$ (Cayman Chemical), were prepared in TSA buffer (150 mM NaCl, 50 mM HEPES, pH 7.4). STING agonists and STING proteins were mixed in three buffer conditions: 1) with 10 mM $MnCl_2$, 2) without $MnCl_2$ (HEPES), or 3) with 10 mM $MnCl_2$ + 100 mM EDTA. The final concentrations of the ligand and protein were 150 and 4 μM, respectively. The mixtures were incubated on ice for 10 min. SYPRO Orange Protein Gel Stain (Sigma–Aldrich) was subsequently added (final 5x concentration) and the mixtures were again incubated on ice for a further 10 min. The protein melting curves were measured with Roche LightCycler QPCR instrument and analyzed by the LightCycler software.

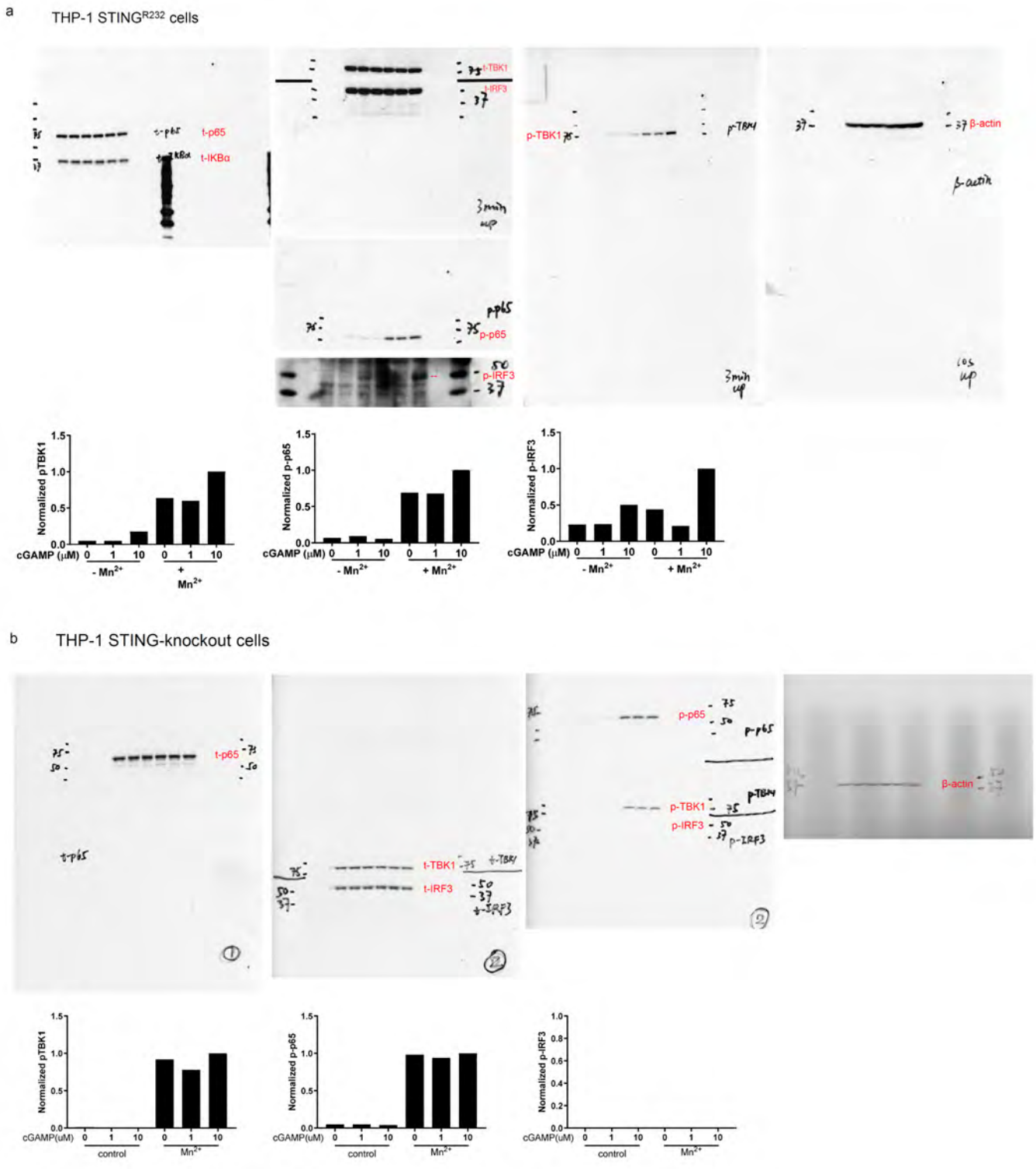

Supplementary Figure 4. Impact of STING agonist + Mn^{2+} on the STING signaling cascade. a) Original uncropped scans and densitometry of Western blotting in **Fig 2f** (THP-1 STING^{R232}, left). **b**, Original uncropped scans and densitometry of Western blotting shown in **Fig 2f** (THP-1 STING knockout, right). Densitometry was quantified by ImageJ. Shown are representative data from two independent experiments with similar results.

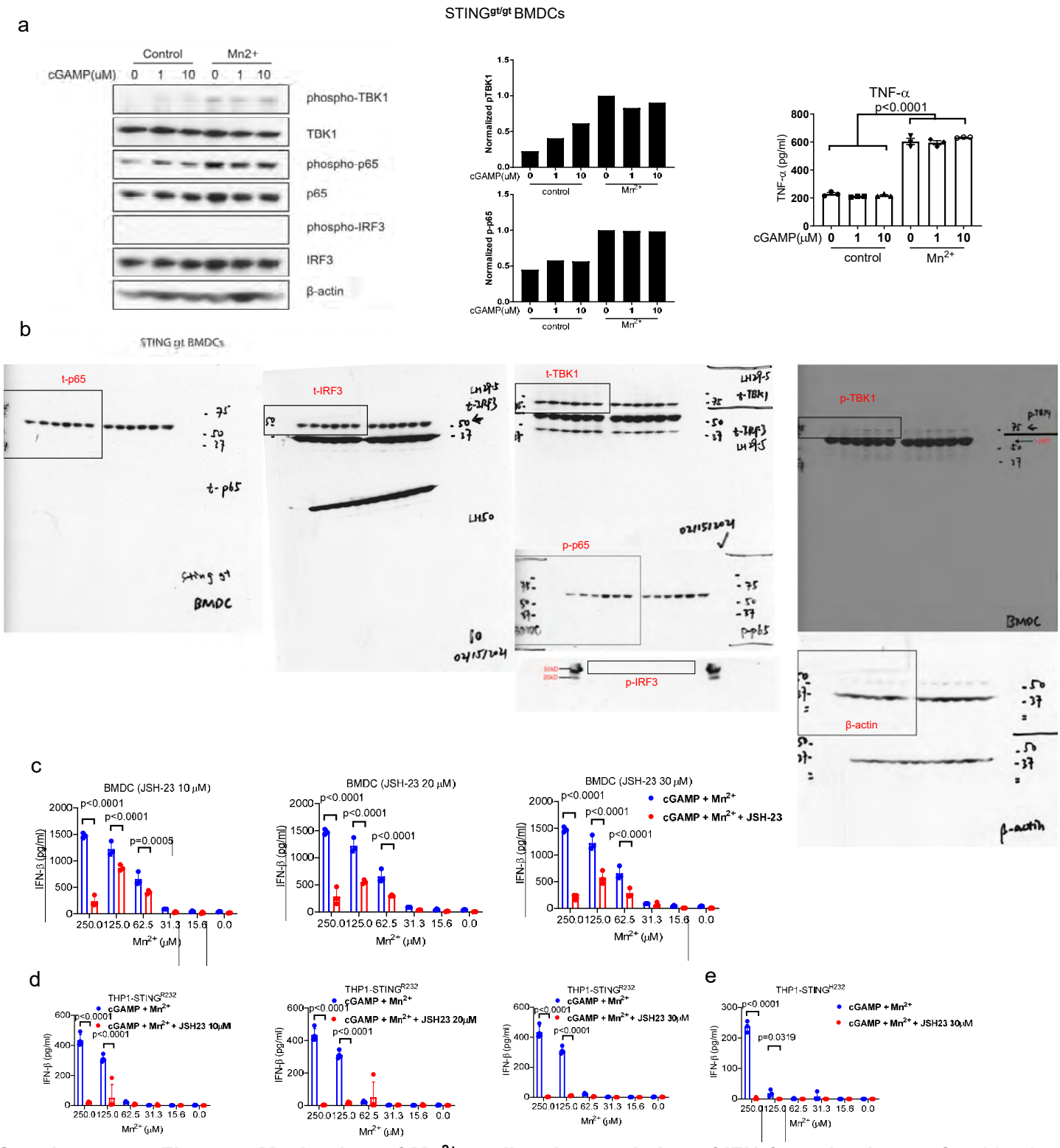

Supplementary Figure 5. Mechanism of Mn^{2+}-mediated potentiation of IFN-β production. a, Combination of STING agonist and Mn^{2+} increased STING-independent TBK1 and p65 phosphorylation in STING$^{gt/gt}$ BMDCs. STING$^{gt/gt}$ BMDCs were harvested from Homozygotes C57BL/6J-Sting1$^{gt/gt}$ mice and prepared according to a previously reported method[9]. STING$^{gt/gt}$ BMDCs were incubated with increasing concentrations of cGAMP with (+ Mn^{2+}) or without 250 μM Mn^{2+} (control) for 6 hours. Cells were lysed in NP40-based buffer in the presence of cocktail proteinase inhibitor and phosphatase inhibitor at 4 °C. Cell lysates were subjected to SDS-PAGE and immunoblotted against marker proteins for STING-IFN-I signaling activation. TNF-α in the cell culture media was measured by ELISA. **b,** Original uncropped scans of Western blotting in (a). Shown are representative data from two independent experiments with similar results. **c-e,** Inhibition of nucleus translocation of p65 reduces Mn^{2+}-

mediated potentiation of IFN-β production. **c,** BMDC cells were incubated with cGAMP and serial concentration of Mn^{2+} in presence or absence of JSH23 (10, 20, 30 μM). After 24 h incubation, IFN-β secretion was quantified by ELISA. **d,** THP-1 THP1 cells expressing $hSTING^{R232}$ were incubated with cGAMP and serial concentrations of Mn^{2+} in presence or absence of JSH23 (10, 20, 30 μM). After 24 h incubation, hIFN-β secretion was quantified by ELISA. **e**, THP1 cells expressing $hSTING^{H232}$ were incubated with cGAMP and serial concentrations of Mn^{2+} in presence or absence of JSH23 (30 μM). After 24 h incubation, hIFN-β secretion was quantified by ELISA. Data represent mean ± SEM, with *n* = 3 biologically independent replicates (a-c). Data were analyzed by two-way ANOVA with Bonferroni's multiple comparisons test.

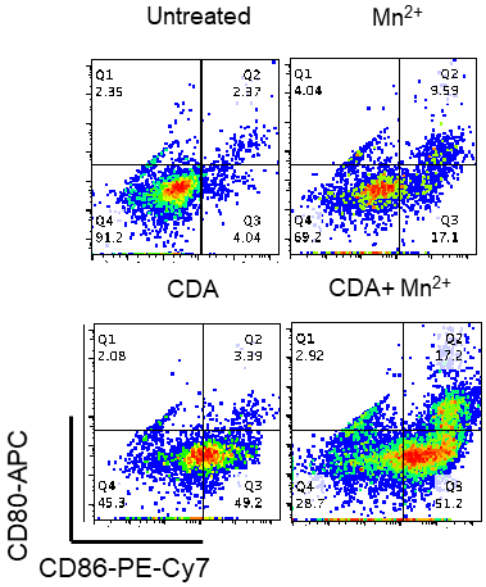

Supplementary Figure 6. Impact of STING agonist + Mn^{2+} on BMDC maturation. As in **Figure 2g**, BMDCs were treated with 5 μM CDA, 250 μM Mn^{2+}, or equivalent amount of CDA + Mn^{2+} for 24 h. CD80 and CD86 were examined by flow cytometry. Shown are the representative scatter plots.

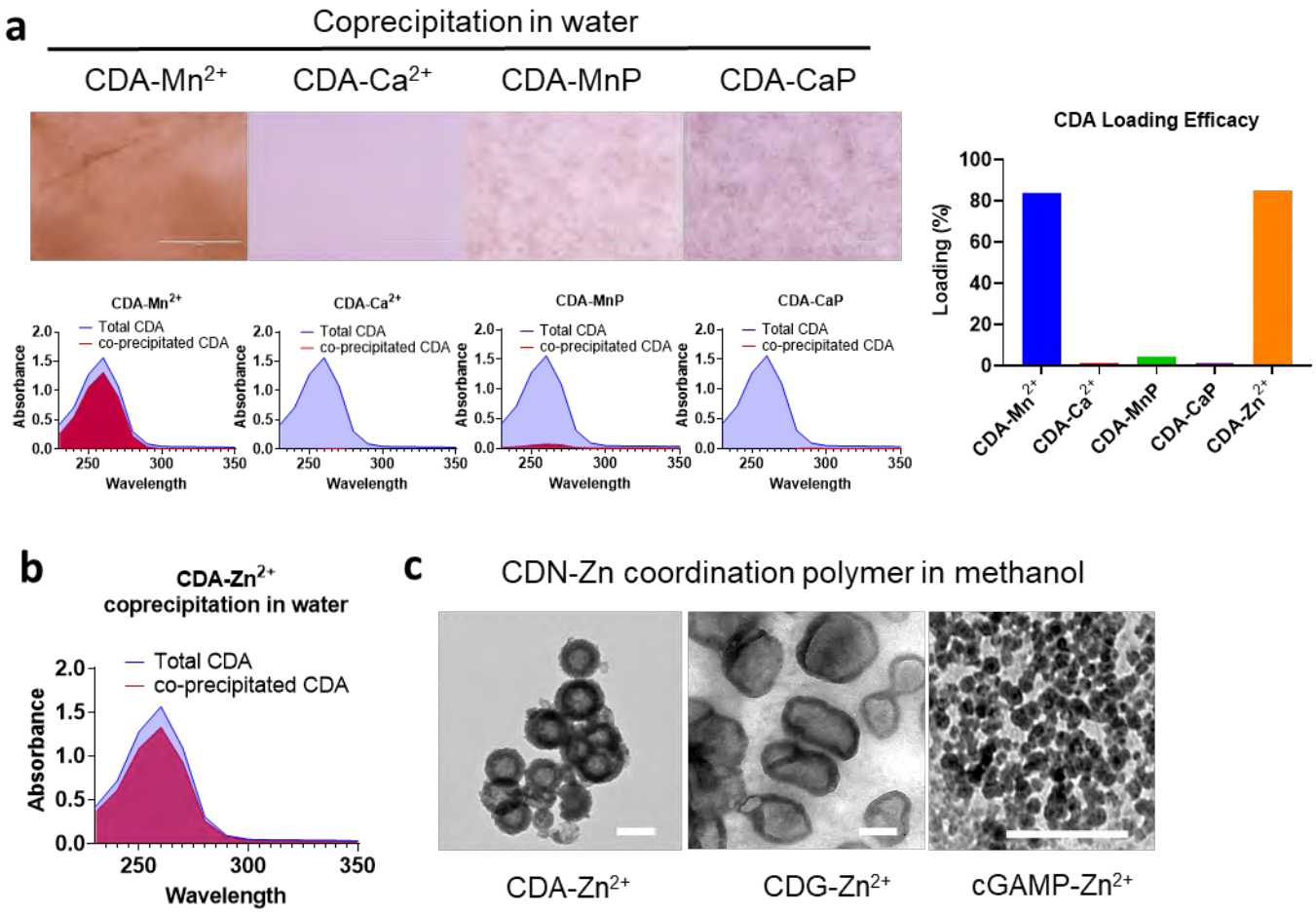

Supplementary Figure 7. Effective coordination of CDNs with Mn^{2+} or Zn^{2+}, but not with Ca^{2+}, Mn-phosphate (MnP) or Ca-phosphate (CaP). a, Mn^{2+} coordinated with CDA and formed visible precipitation under microscope with high drug loading efficacy. In contrast, Ca^{2+}, Mn-Phosphate or Ca-Phosphate failed to coordinate or load CDA. 2 mg/ml CDA were mixed with Mn^{2+} (10:1, n/n) or Ca^{2+} (10:1, n/n) in water while stirring. In parallel, mixed solution of 2 mg/ml CDA and PO_4^{3+} (10:1, n/n) were mixed Mn^{2+} (10:1, n/n) or Ca^{2+} (10:1, n/n) in water while stirring. Total CDA absorbance spectra were measured by a multi-mode microplate reader (BioTek, Synergy Neo2). Shown are the CDA loading efficiencies in the resulting structures. **b,** Zn^{2+} coordinated with CDA and formed visible precipitation under microscope with high drug loading efficacy. 2 mg/ml CDA were mixed with Zn^{2+} (10:1, n/n) in water while stirring. Total CDA absorbance spectra were measured by a multi-mode microplate reader (BioTek, Synergy Neo2). **c,** TEM images of CDN-Zn coordination polymers (CP) formed by mixing CDA, CDG, or cGAMP with Mn^{2+} (10:1, n/n) in methanol while stirring. Scale bars = 100 nm. Shown are representative data from two independent experiments with similar results (a-c).

a Mn^{2+} + CDA in water

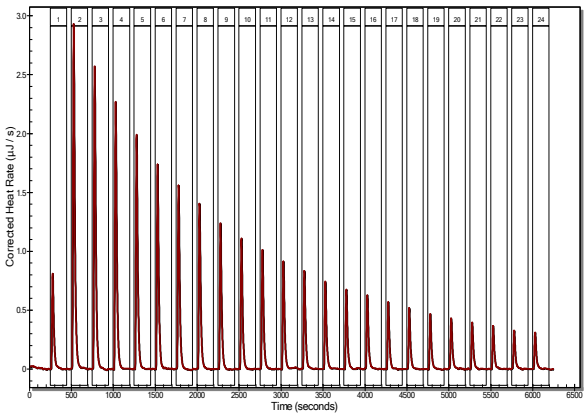

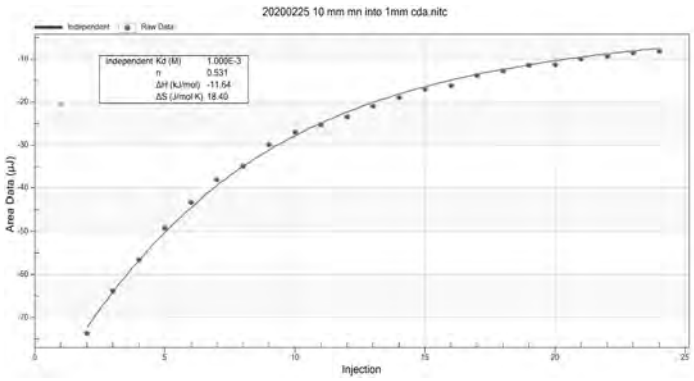

b Mn^{2+} + CDA in methanol

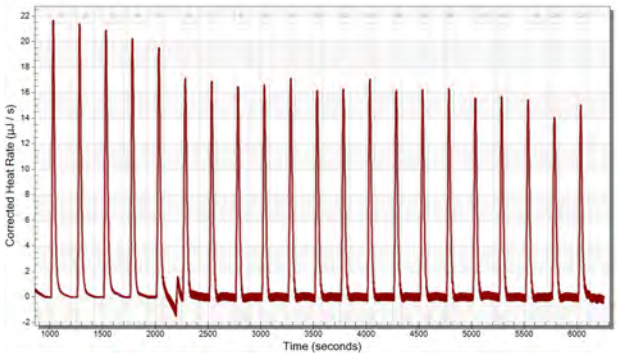

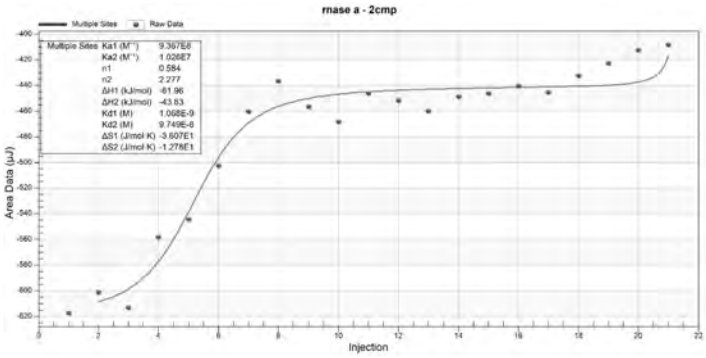

Supplementary Figure 8. a) Isothermal titration calorimetry (ITC) result of titrating Mn^{2+} in water containing CDA. **b**) ITC result of titrating Mn^{2+} into CDA methanol solution.

a

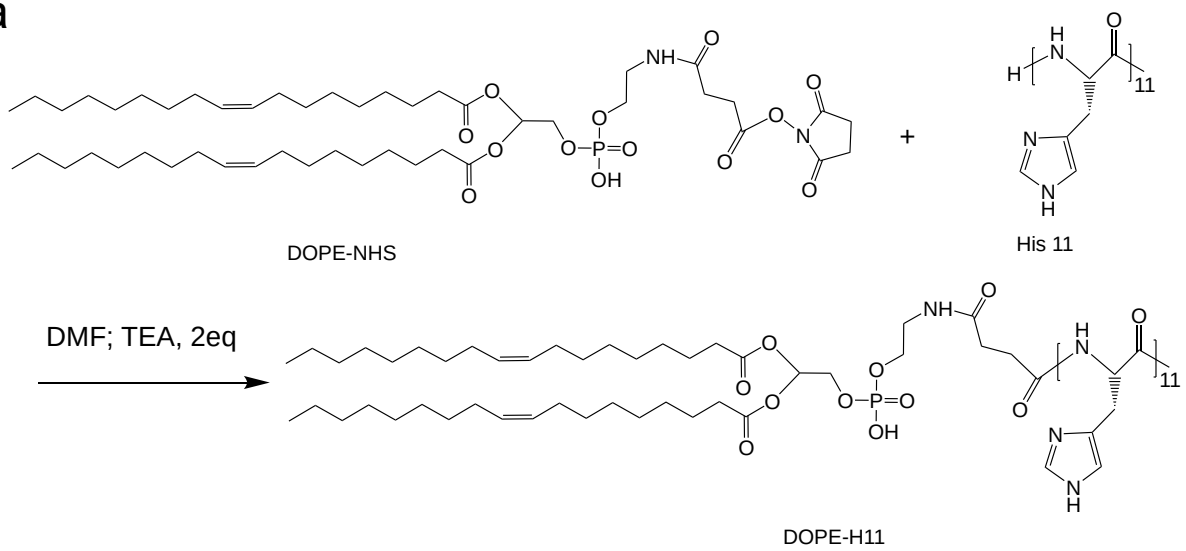

b

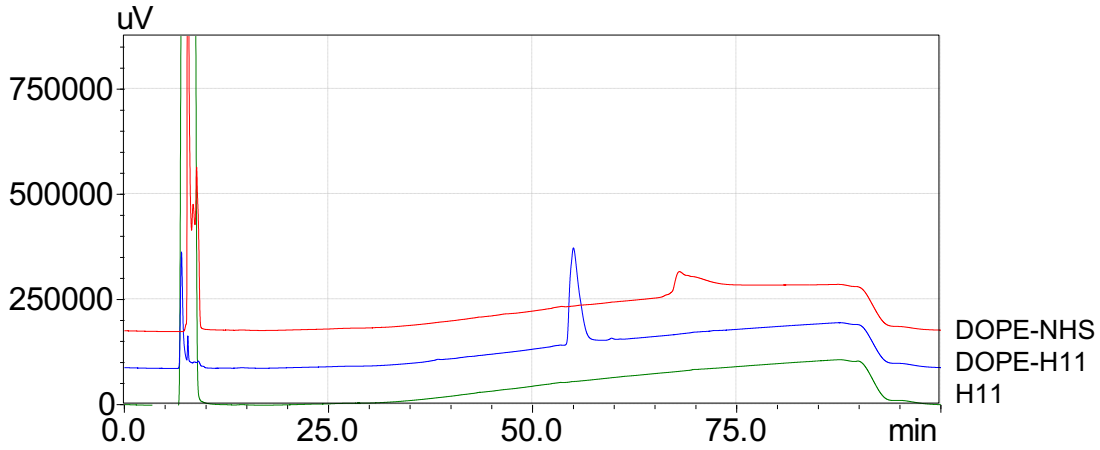

Supplementary Figure 9. a) Synthesis route of DOPE-histidine11 (DOPE-H11). **b)** GPC chromatogram of DOPE-H11.

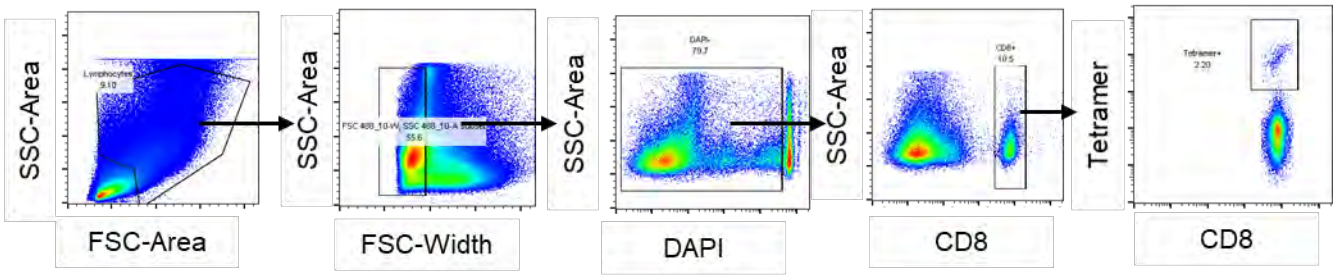

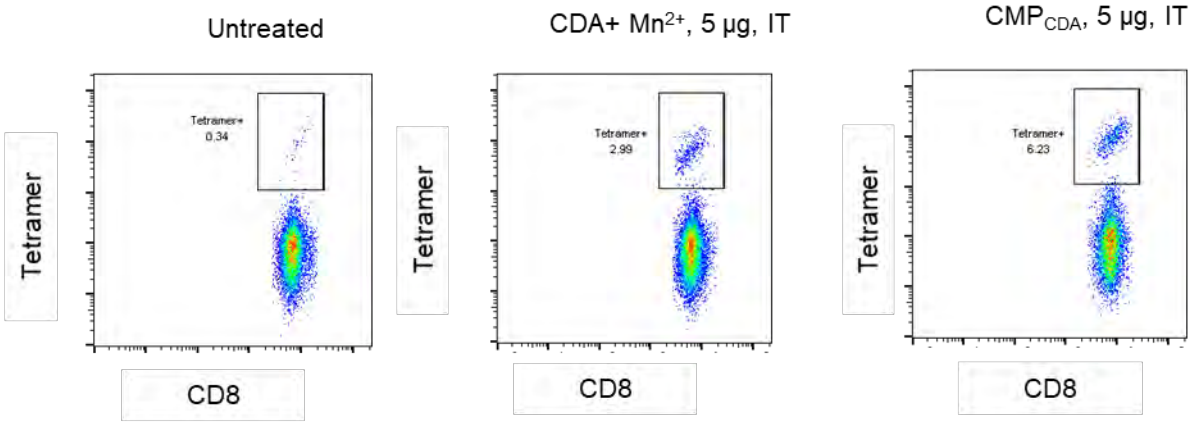

Supplementary Figure 10. Gating strategy for tetramer+ CD8 T-cells and representative scatter plots related to Fig. 4c.

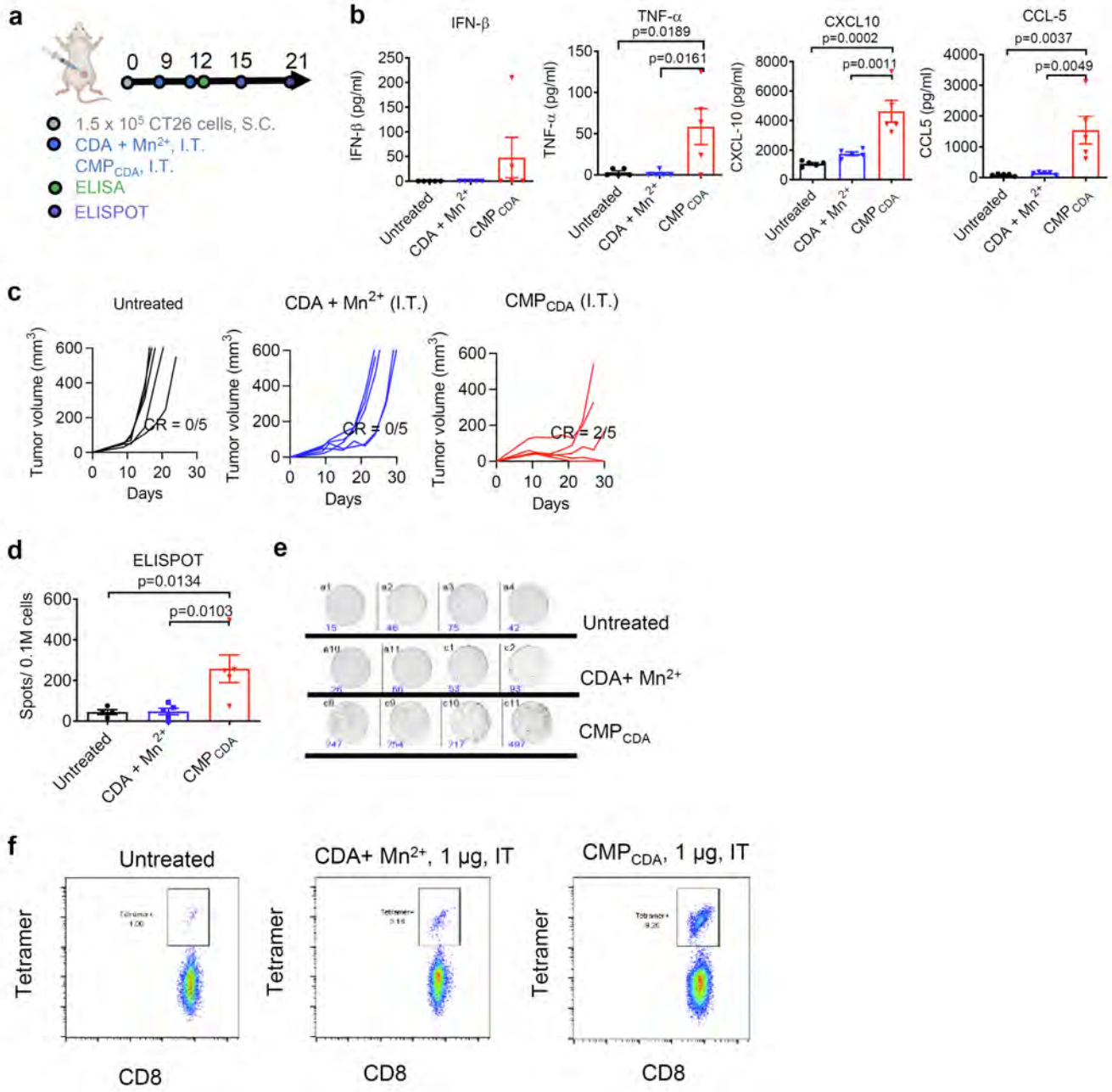

Supplementary Figure 11. Local intratumoral administration of low-dose CMP_{CDA} eliminates established tumors. a) BALB/c mice were inoculated at s.c. flank with 1.5 x 10^5 CT26 tumor cells. CDA+ Mn^{2+} or CMP_{CDA} containing 1 µg CDA and 0.5 µg Mn^{2+} were injected I.T. on days 9, 12, and 15. **b)** Serum cytokines were measured by ELISA at 6 h post the second dose. **c)** Tumor growth was monitored over time. **d-e)** Antigen-specific T cell response in PBMCs was analyzed by AH1-specific IFN-γ ELISPOT assay on day 21. **f)** Representative scatter plots for tetramer+ CD8 T-cells related to **Fig. 4g**. Data represent mean ± SEM, from a representative experiment from 2 independent experiments with *n* = 5 biologically independent samples (b-d). Data were analyzed by one-way ANOVA with Bonferroni's multiple comparisons test.

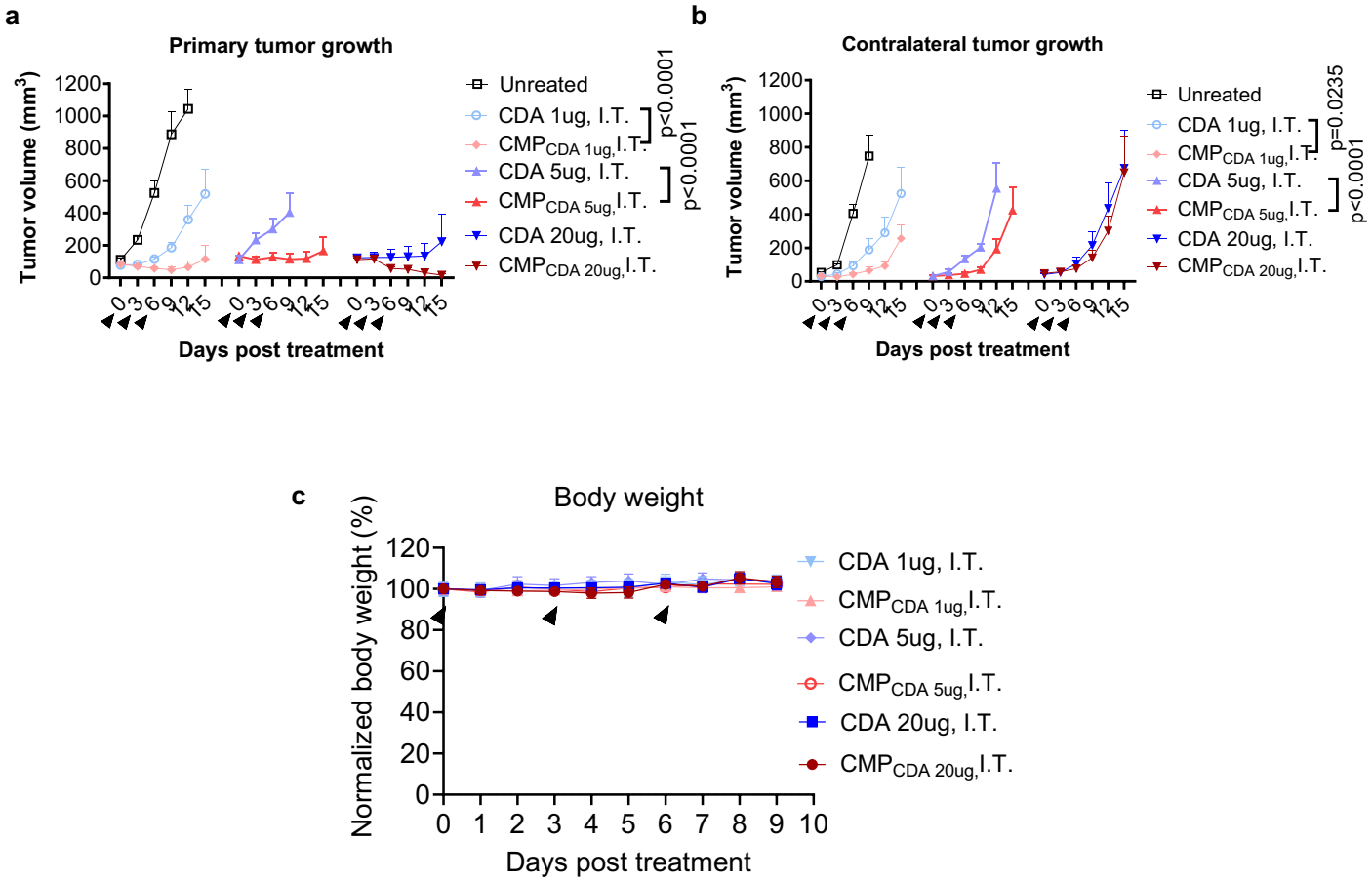

Supplementary Figure 12. Therapeutic effect of CMP in CT26 two-tumor model. a-c, Balb/c mice were inoculated subcutaneously with 3 x 10^5 CT26 tumor cells on the right flank and 1 x 10^5 CT26 tumor cells on the left flank. 3 doses of CDA or CMP_{CDA} containing 1, 5, 20 μg CDA were injected I.T. on the right flank in 3-day intervals when the right tumor size achieve ~100 mm^3. Tumor growth curve of the primary right tumor **(a)** and left distal tumor **(b)** were measured every three days. Body weight change **(c)** is monitored daily. The data show mean ± SEM, with *n* = 5 biologically independent samples (a-c). Data were analyzed by two-way ANOVA with Bonferroni multiple comparisons post-test.

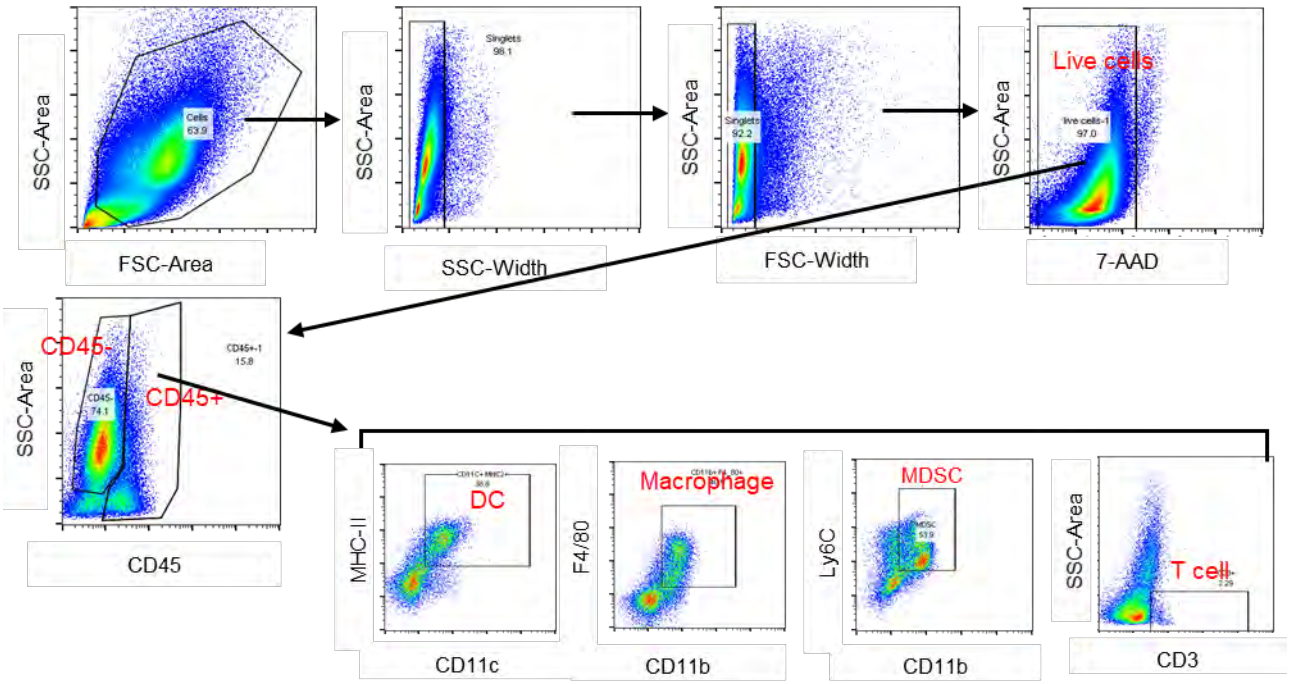

Supplementary Figure 13. Gating strategy for analyzing cellular uptake of CDN in TME related to Fig 4i, 5h.

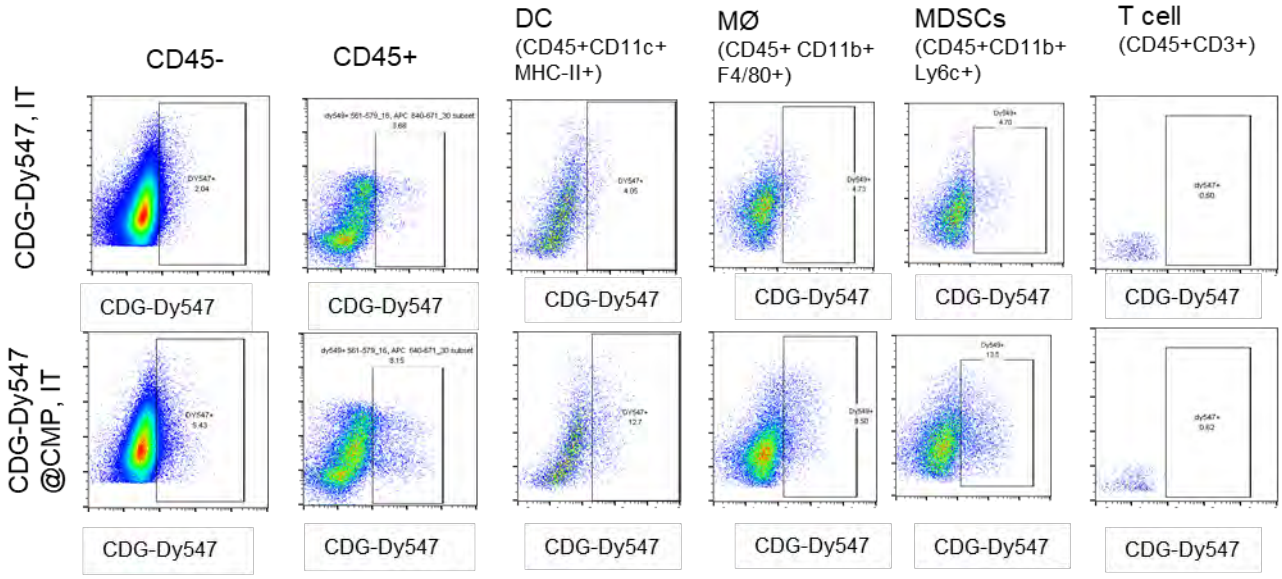

Supplementary Figure 14. Representative scatter plots of CDN distribution in TME after IT injections related to Fig 4i.

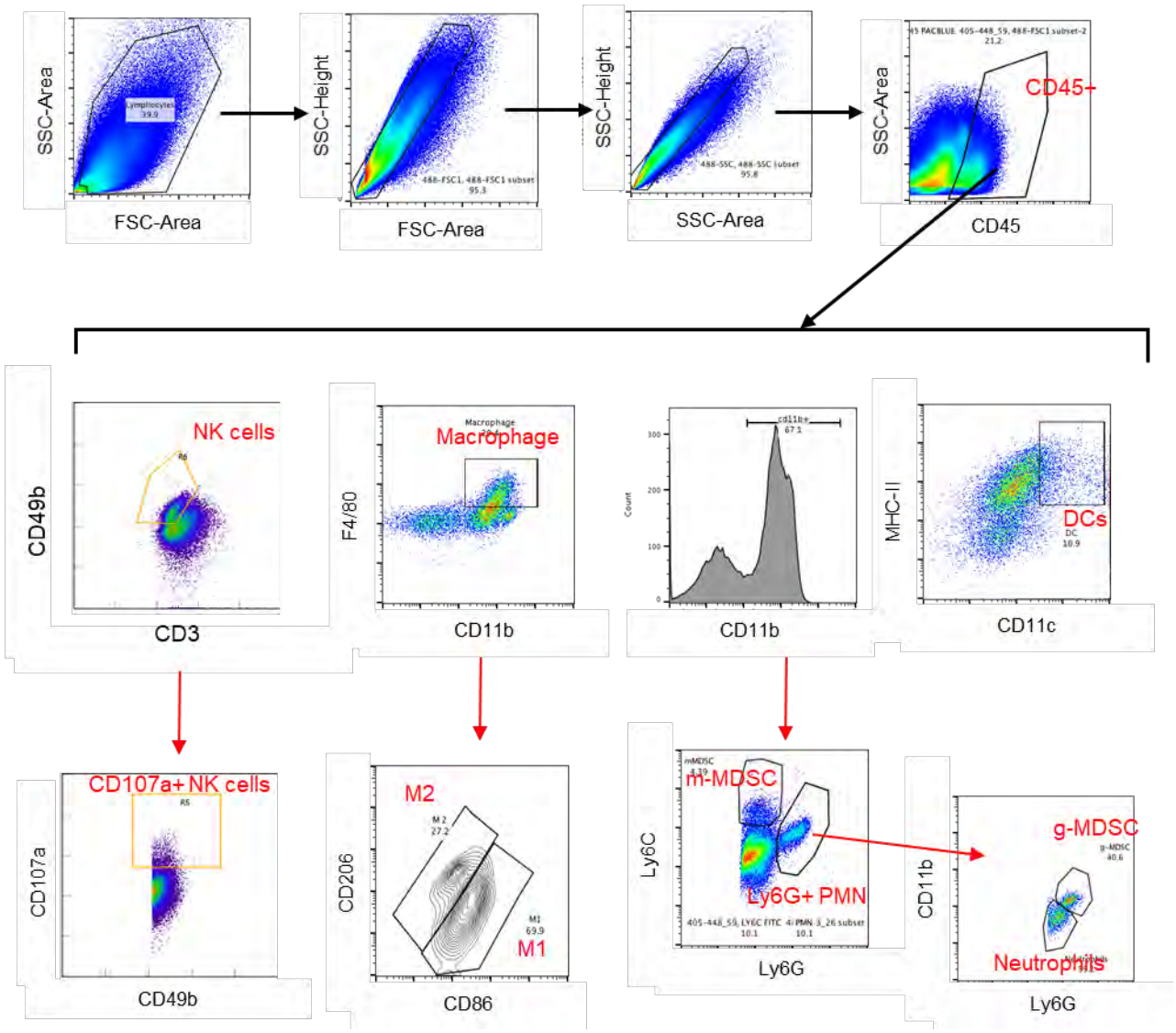

Supplementary Figure 15. Flow cytometry gating strategy for analysis of NK cells, M1-like and M2-like macrophages, DCs, and MDSCs.

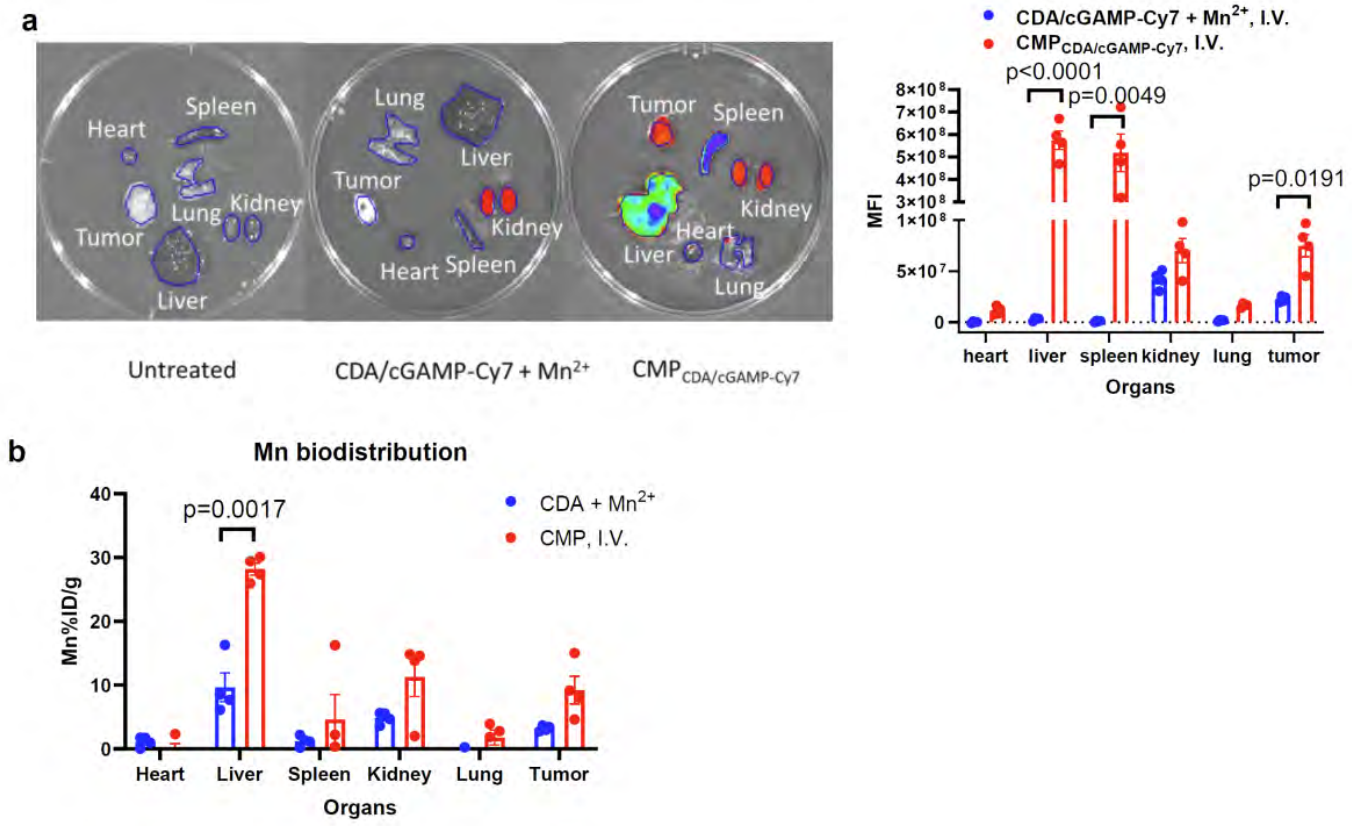

Supplementary Figure 16. Biodistribution of CMP versus CDN + Mn^{2+} after 24 hr of I.V. administration. a, CT26 tumor-bearing mice were injected with $CMP_{CDA/cGAMP-Cy7}$ or free CDA/cGAMP-Cy7 (10:1, n/n) + Mn^{2+}. After 24 hours, mice were euthanized and subjected ex-vivo imaging of major organs using IVIS. Mean fluorescence intensity of each organ was plotted. **b,** Biodistribution of Mn in major organs at 24 h after I.V. injection of free CDA + Mn^{2+} or CMP as measured by ICP-MS. Data represent mean ± SEM (*n* = 4 biologically independent samples) and were analyzed by two-tailed multiple t-test with Bonferroni-Dunn correction (a-b).

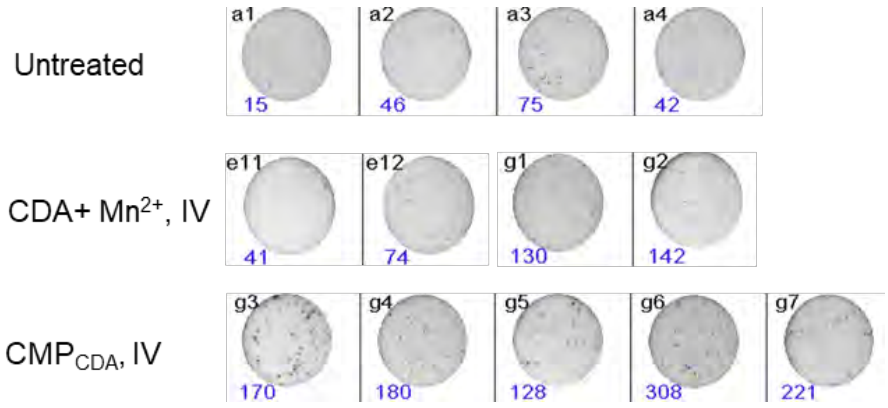

Supplementary Figure 17. Representative ELISPOT images after IV treatments related to Fig. 5c.

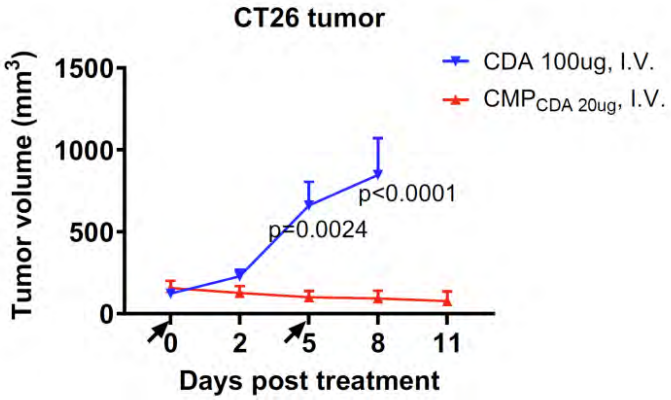

Supplementary Figure 18. Therapeutic efficacy of CMP_{CDA} 20 µg versus 100 µg CDA. BALB/c mice were inoculated subcutaneously with 1 x 10^5 CT26 tumor cells on the right flank. When the tumor size achieved ~100 mm^3, 100 µg CDA or $CMP_{CDA\ 20µg}$ were injected I.V. on day 0 and 5 post the initial treatment. The data show mean ± SEM, with n = 4 biologically independent samples. Data were analyzed by two-way ANOVA with Bonferroni multiple comparisons post-test.

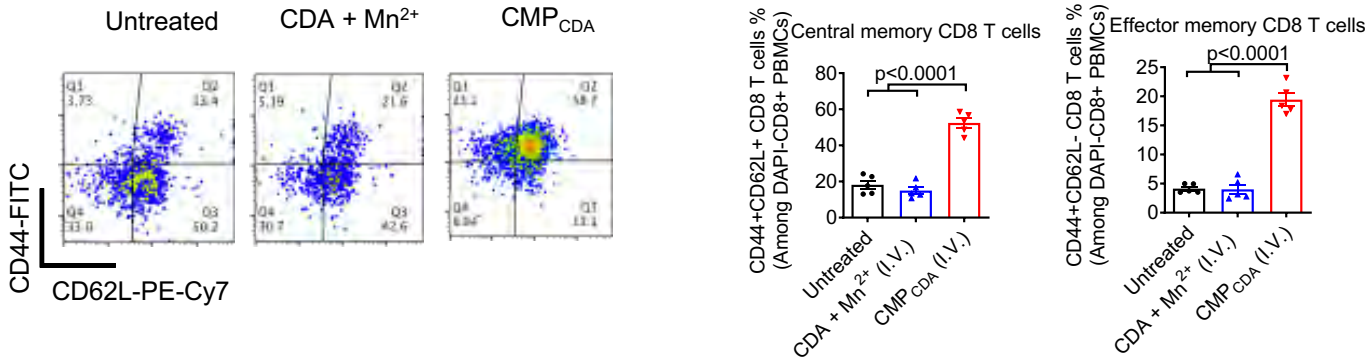

Supplementary Figure 19. Expansion of memory CD8 T cells among PBMCs after I.V. treatment of CMP. BALB/c mice were inoculated at s.c. flank with 1.5 x 10^5 CT26 tumor cells. CDA+ Mn^{2+} or CMP_{CDA} containing 20 µg CDA and 10 µg Mn^{2+} were injected I.V. on days 9, 12, and 15. CD8+ T cells among PBMCs were analyzed by flow cytometry for memory phenotype on day 23. The data show mean ± SEM, with n = 5 biologically independent samples. Data were analyzed by one-way ANOVA with Bonferroni multiple comparisons post-test.

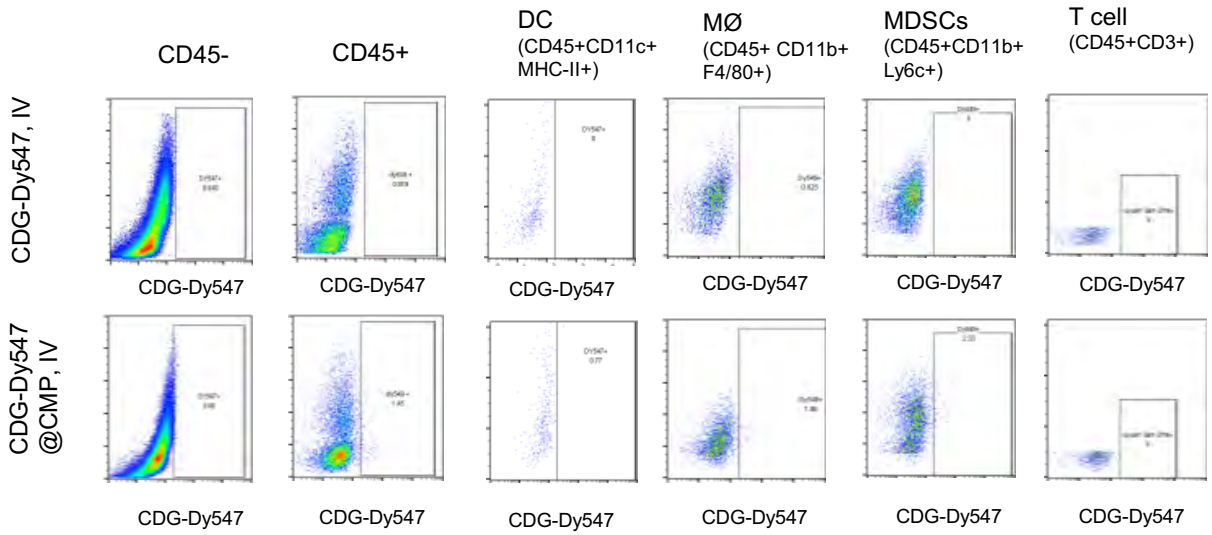

Supplementary Figure 20. Representative scatter plots of CDN distribution in TME after IV injections related to Fig 5h.

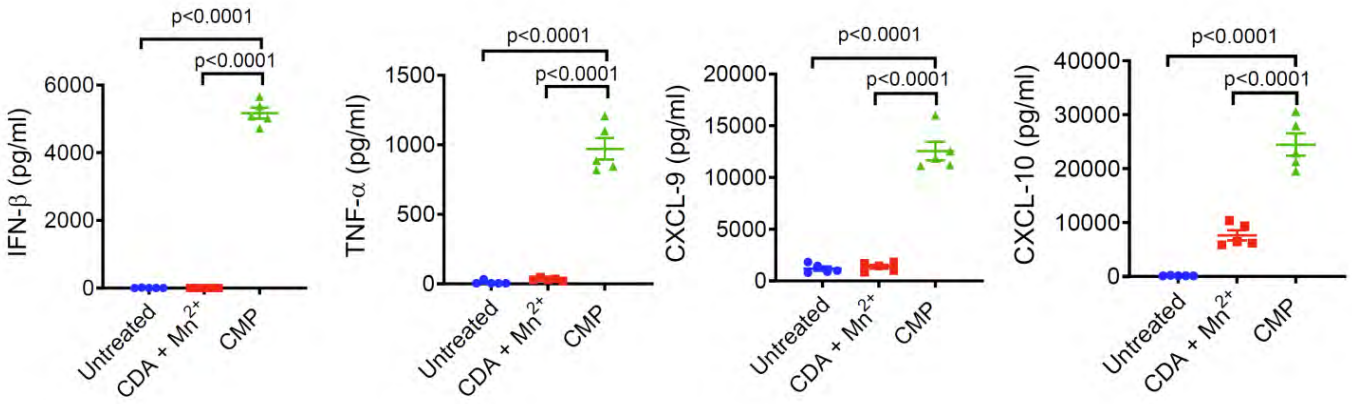

Supplementary Figure 21. B16F10 tumor-bearing mice were treated as in **Fig. 5n**, and serum cytokines were measured by ELISA at 6 h post the second dose. The data show mean ± SEM, with n = 5 biologically independent samples. Data were analyzed by one-way ANOVA with Bonferroni multiple comparisons post-test.

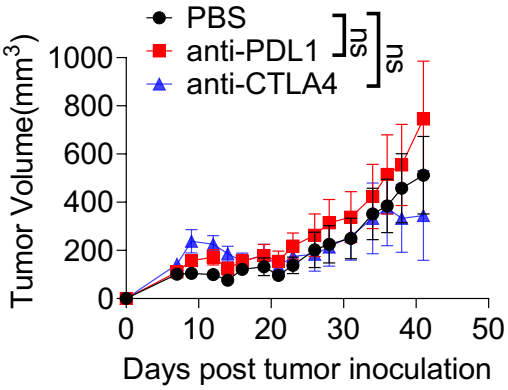

Supplementary Figure 22. Characterization of NOOC1 tumor model. NOOC1 was confirmed to stably produce tumors when implanted in syngeneic C57BL/6J hosts and non-responsive to anti-PDL-1 and anti-CTLA-4 ICB therapy. C57BL mice were inoculated subcutaneously with 2 x 10^6 NOOC1 tumor cells. On day 7, 9, 14,

16, 21, 23 post tumor inoculation, 6 doses of 200 μg anti-PDL1 or anti-CTLA4 in PBS were injected intraperitoneally. Tumor growth was monitored for 40 days **(p)**. The data show mean ± SEM, with n = 6. “ns” indicates no statistical difference, as analyzed by two-way ANOVA with Bonferroni multiple comparisons post-test.

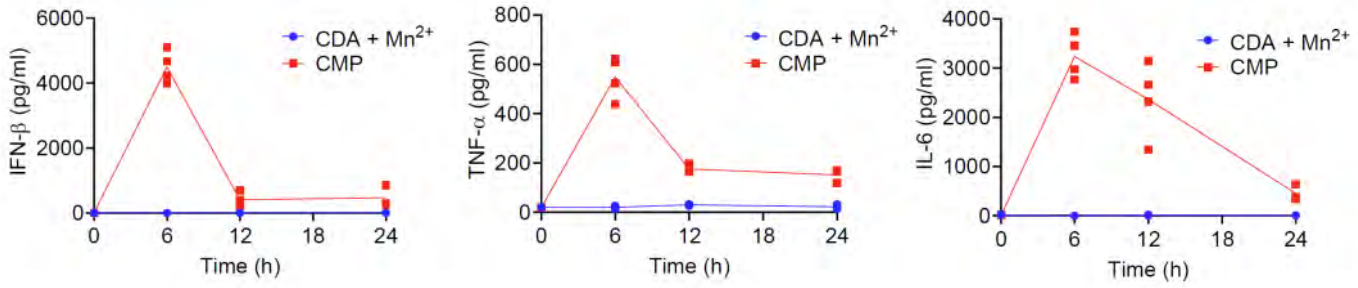

Supplementary Figure 23. Serum cytokine profiles after I.V. therapy with CMP. Serum levels of IFN-β, TNF-α, and IL-6 were measured over 24 hrs after I.V. injection of CMP. The data show mean and individual replicates, with n = 4 biological independent samples.

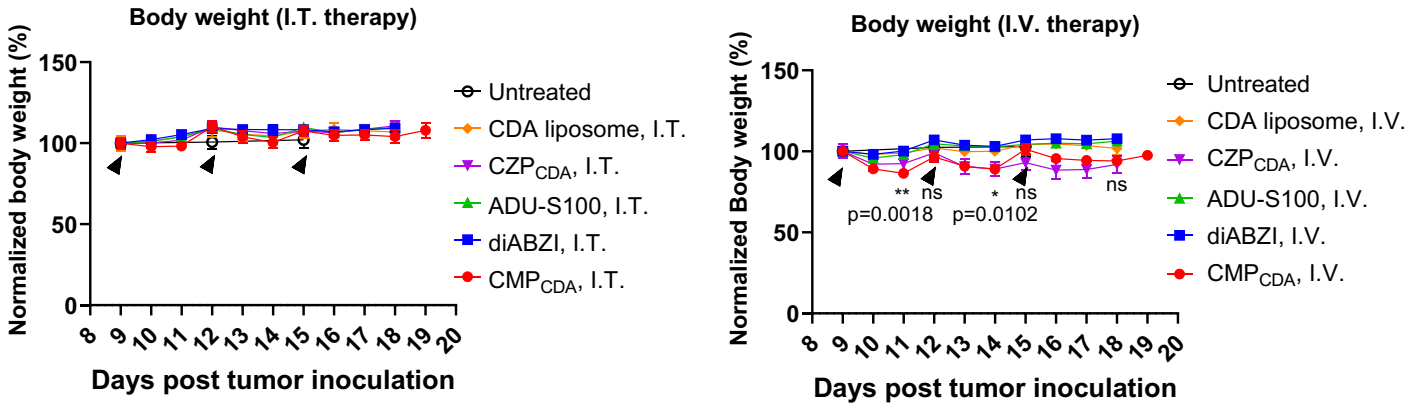

Supplementary Figure 24. Body weight changes over the course of CMP treatment related to Fig 6a-g. The data show mean ± SEM, n=4-5. The results were analyzed by two-way ANOVA with Bonferroni multiple comparisons post-test. * and ** denote statistical significance of CMP$_{CDA}$, I.V., compared with CDA liposome, I.V. “ns” indicates no statistical difference between CMP$_{CDA}$, I.V. and untreated mice.

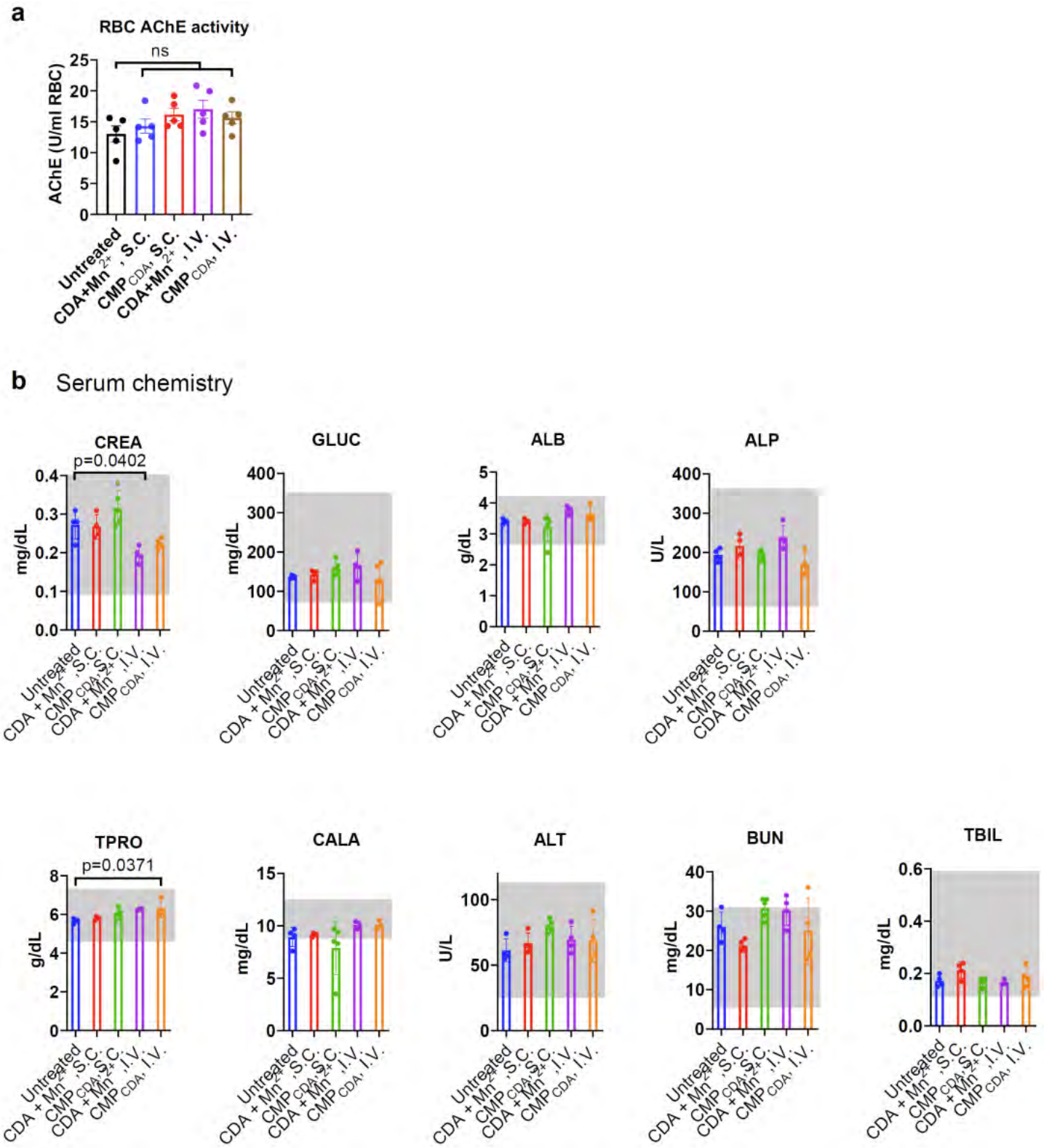

Supplementary Figure 25. Safety assessment of CMP_{CDA} after local or systemic injections. a-b) BALB/c mice were injected with CDA + Mn^{2+} or CMP_{CDA} on days 0, 3, and 6 via S.C., I.T., or I.V. routes. Each injection contained 5 μg CDA and 2.5 μg Mn^{2+} for S.C. or I.T. administration. Each injection contained 20 μg CDA and 10 μg Mn^{2+} for I.V. administration. **a)** Activity of acetylcholine esterase (AChE) in RBC was assessed at 2 h after the last injection. **b)** Serum biochemistry was assayed at 96 h after the last injection. The data show mean ± SEM (n = 4 biologically independent samples) and were analyzed by one-way ANOVA (**a-b**) with Bonferroni multiple comparisons post-test.

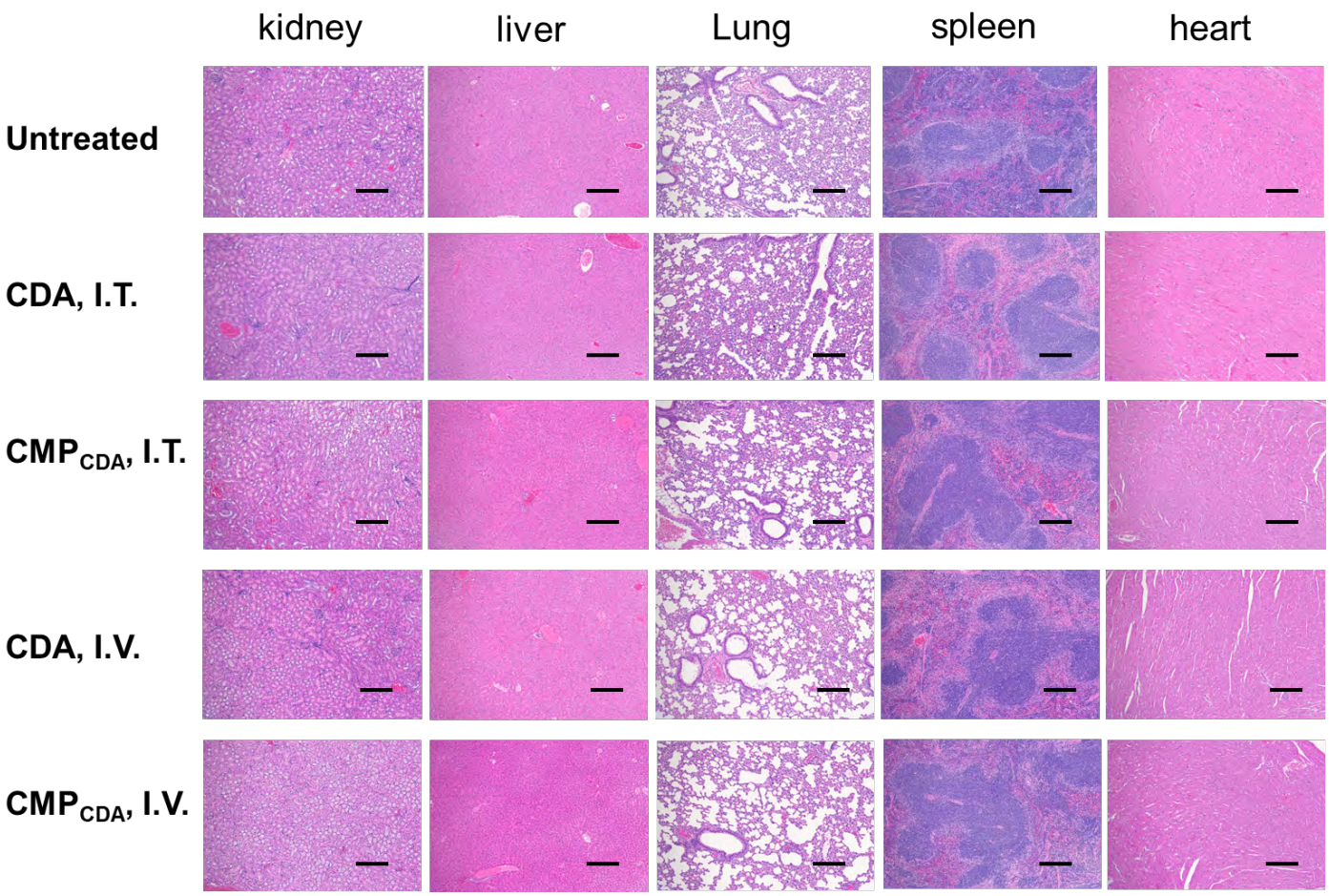

Supplementary Figure 26. Histological analysis of major organs after local or systemic injections of CMP_{CDA}. BALB/c mice were injected with 3 doses of CDA+ Mn^{2+} or CMP_{CDA} either via I.T. (5 μg CDA and 2.5 μg Mn^{2+}) or I.V. (20 μg CDA and 10 μg Mn^{2+}) route of administration with a 3-day interval. One week after the last injection, major organs were harvested for H&E staining and histological analysis. The tissue sections have been examined by a licensed pathologist in a blinded manner. No abnormal histological conditions (inflammation, necrosis, or structure changes) were reported and no differences between groups were observed. Scale bars = 200 μm. Shown are representative images from 4 biologically independent replicates with similar results.

References for the Supporting Information

1 Smola, M., Birkus, G. & Boura, E. No magnesium is needed for binding of the stimulator of interferon genes to cyclic dinucleotides. *Acta Crystallogr F Struct Biol Commun* **75**, 593-598, doi:10.1107/S2053230X19010999 (2019).

2 Li, H. & Durbin, R. Fast and accurate short read alignment with Burrows-Wheeler transform. *Bioinformatics* **25**, 1754-1760, doi:10.1093/bioinformatics/btp324 (2009).

3 Saunders, C. T. *et al.* Strelka: accurate somatic small-variant calling from sequenced tumor-normal sample pairs. *Bioinformatics* **28**, 1811-1817, doi:10.1093/bioinformatics/bts271 (2012).

4 Cibulskis, K. *et al.* Sensitive detection of somatic point mutations in impure and heterogeneous cancer samples. *Nature biotechnology* **31**, 213-219, doi:10.1038/nbt.2514 (2013).

5 Wei, L. *et al.* Ultradeep sequencing differentiates patterns of skin clonal mutations associated with sun-exposure status and skin cancer burden. *Sci Adv* **7**, doi:10.1126/sciadv.abd7703 (2021).

6 Wei, L. *et al.* Whole-genome sequencing of a malignant granular cell tumor with metabolic response to pazopanib. *Cold Spring Harb Mol Case Stud* **1**, a000380, doi:10.1101/mcs.a000380 (2015).

7 Sherry, S. T. *et al.* dbSNP: the NCBI database of genetic variation. *Nucleic Acids Res* **29**, 308-311, doi:10.1093/nar/29.1.308 (2001).
8 Genomes Project, C. *et al.* An integrated map of genetic variation from 1,092 human genomes. *Nature* **491**, 56-65, doi:10.1038/nature11632 (2012).
9 Lutz, M. B. *et al.* An advanced culture method for generating large quantities of highly pure dendritic cells from mouse bone marrow. *J Immunol Methods* **223**, 77-92, doi:10.1016/s0022-1759(98)00204-x (1999).